

ISSP

Activity Report 2004

Contents	Pages
Preface	1
Research Highlights	2 - 27
Highlights of Joint Research	28 - 44
ISSP Workshop	45 - 47
Proposal for Joint Research	48 - 79
Publications	80 - 116



Preface

The ISSP was established in 1957 based on the recommendation of the National Council of Japan to set up a new institute for condensed matter physics. The idea was to establish a top class research institute for experimental and theoretical studies of condensed matter and to promote cooperative research in the field throughout the country. Soon after the inauguration, the name of ISSP became recognized world-wide in the community of condensed matter physics.



Since then there have been two major changes in the history of the institute. The first was the reorganization of the institute in the mid-eighties. The system of divisions consisting of several groups was introduced and the project of the "Physics in extreme conditions", which includes Ultra-High Magnetic Fields, Laser Physics, Surface Physics, Ultra-Low Temperatures, and Very High Pressures, was started. The second major change was the relocation of the ISSP to the new Kashiwa campus which was completed in 2000.

To make the status of the research activities in the ISSP public, new forms were introduced in 2001: Activity report A for research mostly by the staff of the ISSP and Activity report B for joint research conducted by the ISSP. This copy is the Activity Report for the fiscal year 2004 in the style of single volume for all the research activities at the ISSP. The system of national universities in Japan has made a profound change from April in 2004 by the so called "houjinka", which means that national universities, once directly belonged to the ministry of education, have become independent administrative entities. In the new scheme importance of the Activity Report has been increased.

We are happy to receive any comments on the Report for the possible improvement of the research activities of the ISSP.

June 18, 2005

Kazuo Ueda

Director

**Institute for Solid State Physics
The University of Tokyo**

Research Highlights

"Expansion" of SiO₂ Cage Under Pressure

Yagi Group

Many elements and molecules, such as Si, Ge, and H₂O, form clathrate compound, which is composed of cages and included host molecules. Numerous studies have been made to clarify the physical property of these clathrates, because they exhibit a variety of physical properties depending on the combination of cage material and the host molecules. Moreover, one of the H₂O clathrates, methane hydrate, is known as a key material for the energy resource of the next generation and environmental science of the Earth, and the high pressure property of methane hydrate has been studied intensively to clarify its stability. Melanophlogite is a rare natural mineral and has a clathrate structure. It is isostructural with type I gas hydrate and the chemical composition is expressed as 2A•6B•46SiO₂, where A and B are the host molecules in small and large cages, respectively. The cages are formed by SiO₂ network and various gases such as CO₂, CH₄, and N₂ are included in the cage. Little is known on its high pressure behavior and we have studied the stability and compression behavior of this Melanophlogite up to about 25 GPa.

Experiments were made using diamond anvil apparatus, adopting helium as pressure transmitting medium. Helium is known to maintain high hydrostaticity, even above its freezing point of 11 GPa at room temperature. Starting material was a natural sample of melanophlogite from Fortullino, Italy. The Raman spectrum measured on this sample indicates that the main host gas of this sample is CO₂, in harmony with the previous report [1]. For some experiments, this sample was heated in air to 650°C for 7 hours to evacuate the gas from the cage. The intensity of the Raman peak of CO₂ has reduced considerably after this heat treatment, while no change was observed in the Raman peak of SiO₂ network.

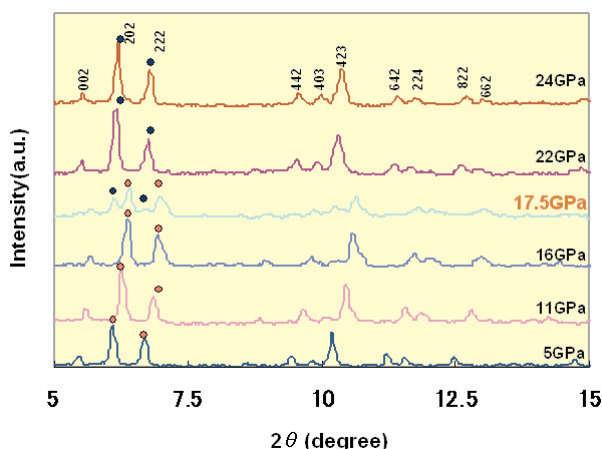


Fig. 1. Powder X-ray diffraction patterns of Melanophlogite with increasing pressure. At 17.5 GPa, new peaks appeared in the low angle region of each peak and then the original peaks have disappeared at higher pressures, indicating that isostructural transition has occurred.

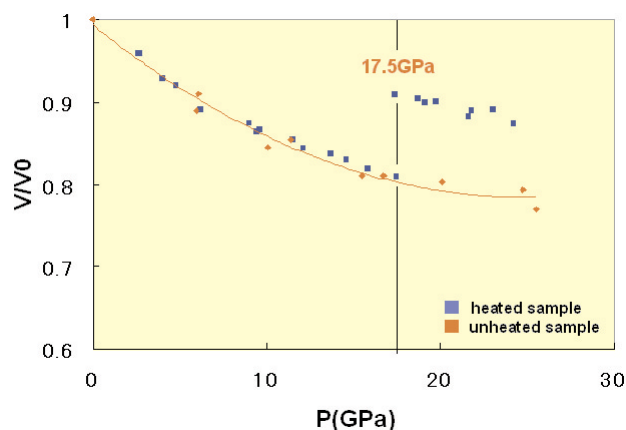


Fig. 2. Volume compression curve of heated and unheated sample of Melanophlogite. No phase transition was observed in unheated sample while sudden increase in volume was found at around 17 GPa in heated sample. This sudden change in volume occurs reversibly in decreasing pressure cycle at about 11 GPa.

No meaningful change was found in the unit cell volume also. Small piece of melanophlogite, cut into rectangular shape of about 50μm × 50μm × 30μm, was placed in the sample chamber together with a small piece of ruby crystal, which works as a pressure marker. Then the chamber was filled with helium and then compressed. X-ray experiments were made at the BL13A station of the Photon Factory, KEK, Tsukuba. Monochromatized synchrotron radiation of about 30 keV energy was collimated to a thin beam of 30μm × 30μm and irradiated to the sample. Diffracted X-ray was recorded using Imaging Plate detector. Typical exposure time was 15 to 30 minutes. Pressure was measured using ruby fluorescence technique.

Monotonous volume compression was observed up to 25 GPa when non-heated sample was compressed at room temperature. The volume has decreased more than 20 % at 25 GPa. On the other hand, when the heated sample was compressed, sudden increase in volume of about 10% was observed at around 17 GPa. Fig. 1 is the X-ray diffraction patterns obtained with increasing pressure. When the pressure was increased to 17.5 GPa, new diffraction lines have appeared in the low angle region of each peak and then the original peaks have disappeared. Diffractions of two phases coexist in a small pressure range of less than 1 GPa. The diffraction pattern above this transition pressure was identical with that before the transition, except the unit cell volume. This sudden change in volume occurs reversibly with large hysteresis, and the volume reverts to original compression curve during decompression at about 11 GPa.

This is a quite unique phase transformation in a sense that it is an isostructural transition and that the volume increases under pressure. It is very likely that helium, which was used as a pressure transmitting medium, have intruded into the cage of melanophlogite and have expanded the volume, although we do not have any direct evidence at this moment.

In another experiment, we have used CH₄ as a pressure transmitting medium and in that case the unit cell volume was compressed much faster and the crystal has changed into amorphous below 10 GPa. Helium is much smaller compared to CH₄ and probably it can penetrate through the SiO₂ network of melanophlogite. The interesting point is that this sudden increase of volume occurs only when the heated sample was used as starting material. In other words, it occurs when the original molecule in the cage has removed and "vacant" cage was compressed by helium. It is likely that helium has intruded into the cage at low pressure and the sudden increase in volume is caused by the additional intrusion of helium. Further studies are required to get information about the number of atoms included in the cage under pressure. Present study provides interesting information on the interaction of cage and host molecule in clathrate compounds.

Reference

[1] H. Gies, Z. Krist., **164**, 247-257(1983).

Authors

T. Yagi, E. Iida^a, H. Hirai^b, N. Miyajima, and T. Kikegawa^c

^a Chuo University

^b Tsukuba University

^c Photon Factory, KEK

A New Puzzle about the Magnetization Plateau in NH₄CuCl₃

Takigawa Group

In some quantum spin systems, the magnetization becomes quantized to a fractional value of the saturation for a finite range of magnetic field. Such magnetization plateaus indicate Mott localization of bosons carrying the magnetization. When the boson density per unit cell is not an integer, a spin superstructure breaking the translational symmetry is generally expected. However, this has been observed so far only in SrCu(BO₃)₂, a frustrated 2D dimer spin system [1]. Another candidate is NH₄CuCl₃, a 3D-coupled dimer spin system, which exhibits magnetization plateaus at 1/4 and 3/4 but not at 1/2 of the full saturation [2]. Since all Cu sites are equivalent in the monoclinic crystal structure (P2₁/c, Fig. 1), the plateaus should be associated with symmetry breaking. However, no evidence has been found for magnetic phase transitions in the field range of the plateaus.

To explain this puzzle, Matsumoto proposed that three types of inequivalent Cu dimers are formed due to yet unob-

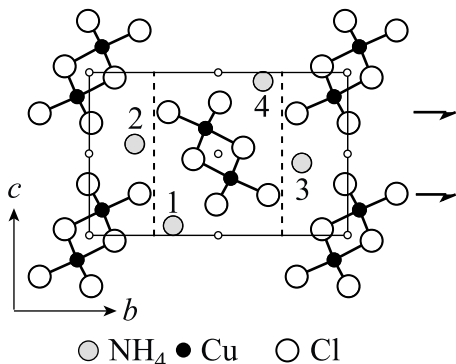


Fig. 1. Crystal structure of NH₄CuCl₃ at room temperature (space group P2₁/c) viewed along the *a*-axis. Zigzag spin chains run along the *a*-axis. Locations of the inversion center, the *b*-screw axes, and the *c*-glide planes are shown.

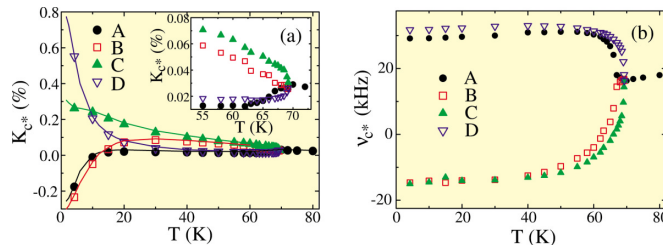


Fig. 2. Temperature dependence of (a) K_{c^*} and (b) ν_{c^*} for the four inequivalent N sites in the low temperature phase at 7 T.

served structural transition [3] and they saturate successively with increasing field. The plateaus appear when every dimer is either in singlet state or completely saturated. Although several experiments support this model, microscopic origin of the plateaus is still unknown.

We have performed ¹⁴N nuclear magnetic resonance (NMR) experiments at the field of 7 tesla where the 1/4-plateau appears at low temperatures [4]. Since ¹⁴N nuclei have magnetic dipole and electric quadrupole moments, ¹⁴N NMR is an excellent probe for both the crystal structure and the spin density distribution. From NMR spectra we obtain the quadrupole coupling ν_{α} , which is proportional to the electric field gradient along the field direction α , and the magnetic hyperfine shift K_{α} from Cu magnetization.

First we observed a small splitting of ν_b below 160 K, indicating a structural transition marginally breaking the *b*-screw and the *c*-glide symmetries but preserving the inversion. Another much more prominent line splitting occurs below $T_c=70$ K. Figure 2 shows the four-fold splitting of K_{c^*} and ν_{c^*} . While ν_{c^*} changes rapidly near T_c , substantial variation of K_{c^*} occurs only at low temperatures. This clearly indicates that what happens at T_c is a structural phase transition, not a magnetic one, most likely associated with orientational order of the NH₄ ions. This would modify the exchange scheme, yielding inequivalent Cu sites with distinct magnetic character. Thus our results support the model by Matsumoto that plateau appears without further symmetry breaking. Figure 2 also indicates a peculiar feature of double transition, which is not understood yet.

For general field directions both K_{c^*} and ν_{c^*} show eight-fold splitting. Their angular dependences are approximately symmetric about the *ac*-plane within two degrees, indicating that *c*-glide symmetry is still only marginally broken. Meanwhile, Rüegg *et al.* observed doubling of the unit cell along the *b*-axis by neutron diffraction [5]. A unit cell of the low temperature phase then contains eight Cu sites, which is the same as the number of NMR lines for the general field directions. Thus, the space group should be P1 and the inversion symmetry must be completely broken.

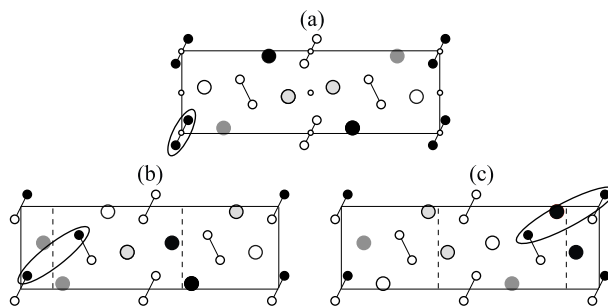


Fig. 3. Possible spin structure for the 1/4-plateau state. The small filled (open) circles indicate the triplet (singlet) Cu sites. Large circles show the N sites. The dashed lines in (b) and (c) indicate the approximate *c*-glide planes preserved in each spin configurations.

We now have ample evidence that in the 1/4-plateau 1/4 of Cu spins form fully polarized triplets while the rest remain in singlet. The question then is where the triplets are. All previous studies assume the triplets on the nearest neighbor pairs as shown in Fig. 3(a). This configuration, however, preserves the inversion but completely destroys the c -glide symmetry inconsistent with NMR results. To satisfy the approximate c -glide symmetry, the triplets must be formed over different chains as shown in Fig. 3 (b) and (c). Such configuration would require extremely peculiar exchange coupling scheme. Our NMR results have posed a new puzzle about the spin superstructure in NH_4CuCl_3 .

References

- [1] K. Kodama *et al.*, *Science* **298**, 395 (2002).
- [2] W. Shiramura *et al.* *J. Phys. Soc. Jpn.* **67**, 1548 (1998).
- [3] M. Matsumoto, *Phys. Rev. B* **68**, 180403 (2003).
- [4] K. Kodama *et al.*, *Prog. Theor. Phys. Suppl.*, submitted.
- [5] Ch. Rugg *et al.*, *Phys. Rev. Lett.* **93**, 037207 (2004).

Authors

K. Kodama, M. Takigawa, and H. Tanaka^a
^a Tokyo Institute of Technology

Contrasting Spin Dynamics in the Family of β -Pyrochlore Osmate Superconductors

Takigawa and Hiroi Groups

Quantum spins on the pyrochlore lattice, a network of corner-shared tetrahedra, have attracted strong recent interest, because the frustrating interactions may lead to an exotic RVB spin-liquid ground state. To understand the behavior of itinerant electrons on such a lattice is a challenging issue. Anderson's proposal that the RVB-singlet state would evolve into a superconducting state by carrier doping motivated experimental efforts to find superconductors on frustrated lattices. In 2004, Yonezawa, Muraoka, and Hiroi at ISSP discovered a new family of osmates superconductors AOs_2O_6 ($A=\text{K, Rb, Cs}$), where the Os sites form a pyrochlore lattice [1] (see the ISSP Activity Report 2003). It is particularly attractive that different alkaline elements lead to large variation of the superconducting transition temperature T_c , which is 9.6 K, 6.3 K, and 3.3 K for $A = \text{K, Rb, and Cs}$, respective-

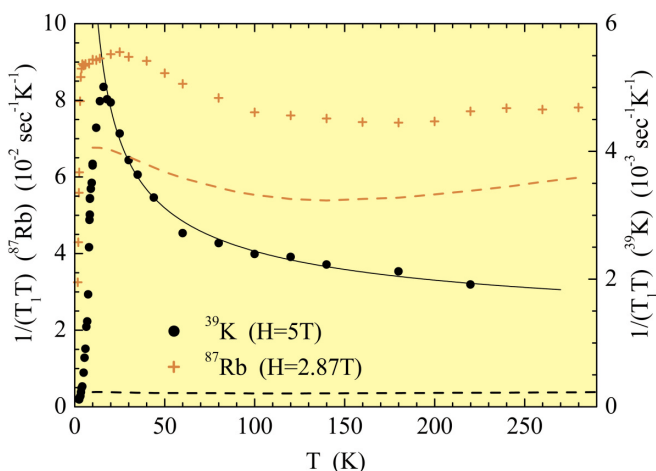


Fig. 1. Temperature dependence of $1/T_1T$ in RbOs_2O_6 (red symbol, scale on the left axis) and KOs_2O_6 (black symbol, scale on the right axis). Dashed lines show the Knight shift data. The solid line shows the fitting to the spin fluctuation theory for nearly antiferromagnetic metals.

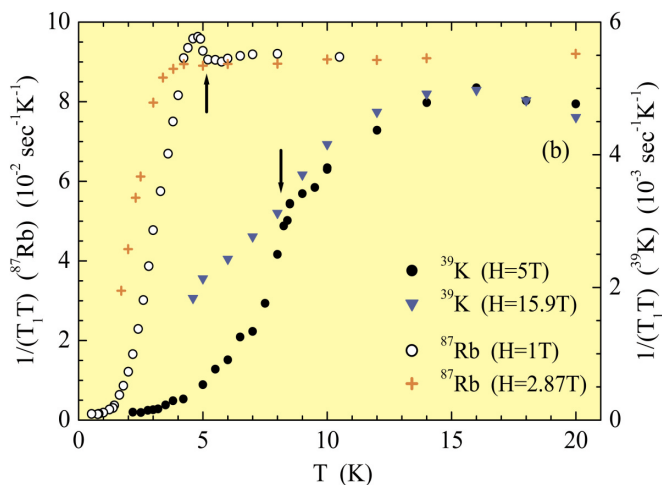


Fig. 2. Temperature dependence of $1/T_1T$ in the low temperature region. The pseudo-gap behavior in KOs_2O_7 is virtually unchanged when the field is increased. A small Hebel-Slichter peak immediately below T_c is observed in RbOs_2O_7 at low field but not in KOs_2O_7 .

ly. This may allow us to identify what determines T_c .

We have performed nuclear magnetic resonance (NMR) experiments on ^{39}K nuclei in KOs_2O_7 and on ^{87}Rb nuclei in RbOs_2O_7 . We found remarkably contrasting magnetic and superconducting behavior for the two materials. The temperature dependence of the nuclear spin-lattice relaxation rate divided by temperature ($1/T_1T$) is shown in Fig. 1. The spin-lattice relaxation is dominantly caused by the spin fluctuations of Os-5d electrons. If the spatial spin correlation is absent, $1/T_1T$ is determined from the static spin susceptibility or the Knight shift by the Korringa relation. This result is shown by the dashed lines for KOs_2O_7 (black) and RbOs_2O_7 (red). While the experimental data of $1/T_1T$ is only modestly enhanced over the Korringa result in RbOs_2O_7 , it is strongly (more than ten times) enhanced in KOs_2O_7 . We also note that $1/T_1T$ is strongly temperature dependent only for KOs_2O_7 . This temperature dependence is consistent with the spin-fluctuation theory for nearly antiferromagnetic metals in three dimension (solid line).

Striking difference appears also in the low temperature behavior as shown in Fig. 2. For KOs_2O_7 , $1/T_1T$ shows a peak near 16 K, which is twice as large as T_c at the magnetic field of 5 T used for this measurements. This resembles the so-called "pseudo-gap" behavior observed in cuprate high temperature superconductors in the underdoped region. It indicates depression of the low energy spin fluctuations as if singlet pairing takes place even in the normal state. However, the behavior remains unchanged when the field is increased to 16 T which reduces T_c to almost a half. Therefore, superconducting fluctuations must be irrelevant. Below T_c , a weak Hebel-Slichter peak is observed in RbOs_2O_7 but not in KOs_2O_7 .

A possible origin for the contrasting properties of the two compounds is the subtle difference in the shape of Fermi surface and different degree of nesting as suggested from the band structure calculation by Harima.

References

- [1] S. Yonezawa *et al.*, *J. Phys.: Condens. Matter* **16**, L9 (2004).
- [2] K. Arai *et al.*, *cond-mat/0411460*.

Authors

K. Arai, J. Kikuchi, K. Kodama, M. Takigawa, S. Yonezawa, Y. Muraoka, and Z. Hiroi

Modulated Quadrupole Ordering in PrPb₃

Sakakibara and Yoshizawa Groups

Because of a strong intra-atomic spin-orbit coupling, the orbital degeneracy in *f* electron systems is described in terms of quadrupole moments which are rank-2 tensor operators of the total angular momentum *J*. The orbital ordering in *f* electron systems, i.e., a spontaneous lifting of the orbital degeneracy by interactions, therefore is a phase transition of quadrupole moments. Following magnetic orderings, one refers to uniform alignment of the quadrupole moment as a ferroquadrupolar state, whereas an ordering having a staggered quadrupolar component is called an antiferroquadrupolar (AFQ) state.

The AFQ ordering systems whose ordering structure has been identified are still limited in number. All the AFQ structures known so far have simple *q* vectors (simple alternations of the quadrupole moments). One of the reasons for this could be the short-range nature of quadrupolar interactions. Nevertheless, it has been argued theoretically that an indirect quadrupolar interaction of RKKY-type might exist in some intermetallic systems; the existence of long-range quadrupolar interactions would not rule out the possibility of modulated or incommensurate AFQ structures.

Here we report on our recent study on the AFQ structure of the cubic intermetallic compound PrPb₃. The 4*f* electrons of this compound are almost localized, having an orbitally degenerate level in the crystalline electric field ground state. PrPb₃ is known to exhibit a second order phase transition at 0.4 K, which has been considered (but not confirmed microscopically) as an AFQ transition. Very recently, we have succeeded in identifying the AFQ structure of PrPb₃ by means of neutron scattering measurements in a magnetic field [1]. To our surprise, the ordered state turns out to be a long-period modulated quadrupole phase.

Figure 1 shows the results of the *Q* scans performed in a field of *H*=4 T applied parallel to the [001] axis. Clear magnetic superlattice reflections are observed at *q*=(1/2± δ 1/2 0), δ ~0.125 below the AFQ transition temperature *T*_Q~0.65 K. These reflections are distinguished from the ordinary antiferromagnetic ones because their intensity continuously decreased with decreasing field and vanished at

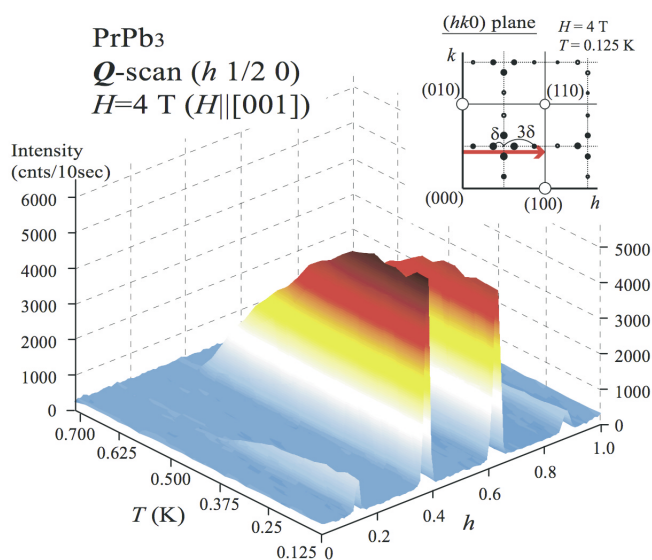


Fig. 1. Results of the (*h* 1/2 0) scans in a field of 4 T applied parallel to the [001] axis. Inset shows the magnetic (solid circles) and nuclear (open circles) reflections observed at 0.125 K.

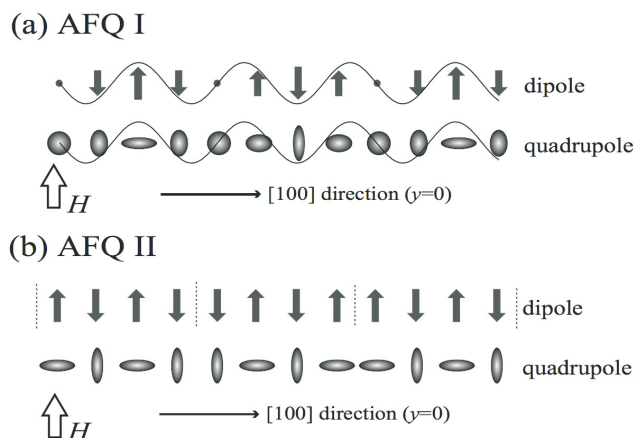


Fig. 2. Obtained magnetic (arrows) and quadrupole (ovals) structures of PrPb₃. The antiferromagnetic moment appears when an external field is applied to the AFQ state. AFQ-I is the modulated structure observed below *T*_Q, which turns into the antiphase structure (AFQ-II) at low temperatures in a field above 1 T.

H=0. This behavior is exactly what one would expect for the AFQ phase. Below ~0.4 K, 3rd harmonic reflections are observed at *q*'=(1/2±3 δ 1/2 0), indicating the structure turns into a square shape at low *T*.

The magnetic and quadrupole structures of PrPb₃ obtained from the present measurements are shown in Fig. 2, where the ovals and the arrows indicate the expected quadrupole and induced magnetic structures, respectively. Generally, in an AFQ phase, an antiferromagnetic (AF) component compatible to the AFQ order parameter (OP) is induced in a field and gives rise to magnetic superlattice reflections. Below *T*_Q, the induced AF moment parallel to [001] has the long-period modulated structure as shown in Fig. 2(a) (AFQ-I). The underlying AFQ moment is also expected to have the long-period modulation. This is the *first observation* of the quadrupolar ordering with a long-wavelength amplitude modulation. The AFQ OP is determined to be of *O*₂⁰ type ($=2J_z^2 - J_x^2 - J_y^2$) from the polarization of the induced AF component. At lower temperatures and above 1 T, this state undergoes a 1st-order transition to an antiphase square structure denoted as AFQ-II in Fig. 2(b). Very interestingly, the non-square modulated phase AFQ-I is found to persist as *T*→0 at low field below 1 T. This observation suggests that the local quadrupole moment of Pr³⁺ is partially quenched by hybridization with conduction electrons (*quadrupole Kondo effect*).

Reference

[1] T. Onimaru *et al.*, Phys. Rev. Lett. **94**, 197201 (2005).

Authors

T. Onimaru, T. Sakakibara, N. Aso, H. Yoshizawa, H.S. Suzuki^a, and T. Takeuchi^b
^a National Institute of Materials Science
^b Osaka University

Studies on BIODE (Biomolecular light-emitting diode)

Tajima and Akiyama Groups

A thin-film organic light-emitting diode (OLED) was fabricated by Vincett *et al* for the first time [1]. This device is of interest not only for the practical use but also for the

basic research. By fabricating this device, we can measure the electro-luminescence (EL) spectra of the insulating organic compounds, and can study their electrical and optical properties simultaneously.

Recently, we have succeeded in fabricating OLED's from heme proteins (cytochrome *c* and myoglobin) [2, 3] and chlorophyll *a* [4]. This is the first report on the fabrication of the biomolecular light-emitting diode ("BIOLED"). Heme proteins do not or hardly exhibit photo luminescence. In this respect, the mechanism of EL in heme proteins are of interested not only for bioscience but also for physics.

Figure 1a and 1b show the current and EL intensity simultaneously measured for a cytochrome-*c* BIOLED. The two characteristics are plotted as a function of the biased voltages applied to the electrodes. The voltage was increased from zero to ~14 V and then reduced to zero in one cycle. This voltage cycle was repeated four times. As can be seen from the figure, both the current and EL intensity are not reproducible even for one sample. The external quantum efficiency of the EL spectrum is defined as a probability that a single photon is emitted when a single electron pass across the OLED junction. This quantity is proportional to the EL intensity and inversely proportional to the current. Figure 1c shows the quantum efficiency, thus obtained, plotted as a function of the applied voltages. Interestingly, the external quantum efficiencies evaluated from the current and EL intensity shown in Figs. 1a and 1b are reproducible for all the voltage cycles. Moreover, this quantity is consistent within 20 % error in all the cytochrome *c* devices measured.

Figure 2 shows a schematic energy diagram of the ITO/ferricytochrome *c*/Al junction determined from UPS and optical measurements. The oxidized cytochrome *c* has a hole in the d_{yz} orbital, while the lower d_{xy} and d_{xz} orbitals are fully occupied. This energy diagram shows that the Al cathode has closer work function to the Fe d_{z^2} orbital than to the

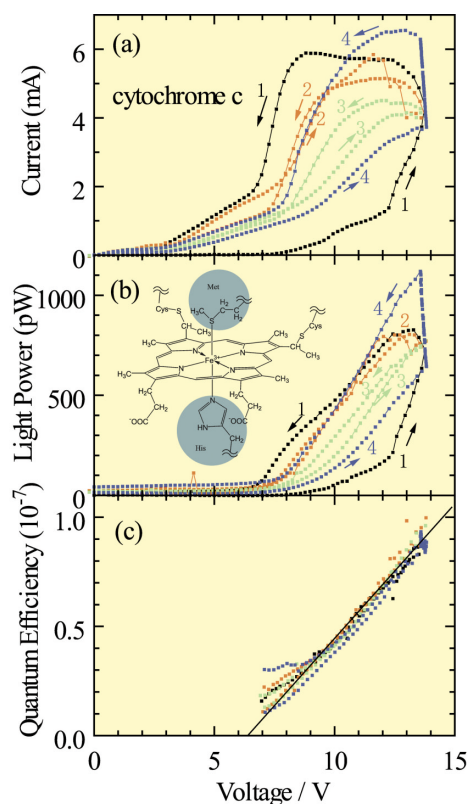


Fig. 1. Current-voltage characteristics (a), EL intensity-voltage characteristics (b), and quantum efficiencies (c) for cytochrome *c*. Quantum efficiencies are evaluated from the data shown in (a) and (b). The inset shows the molecular structure of cytochrome *c*.

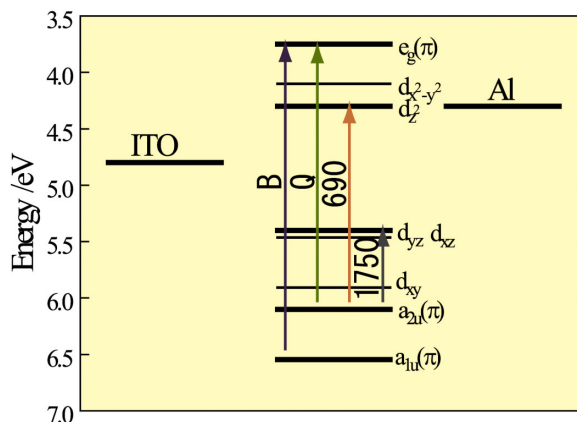


Fig. 2. The Schematic energy diagram of ITO/ferricytochrome *c*/Al junction. [B: Soret band; Q: Q band; 690: 690 nm band; 1750: 1750 nm band (MCD)] The energy levels of $e_g(\pi)$, d_z^2 , d_{yz} , $a_{2u}(\pi)$, $a_{1u}(\pi)$ are estimated on the basis of the work function given by UPS spectroscopy and assignment of optical transitions. The levels of $d_{x^2-y^2}$, d_{xz} , d_{xy} are not determined.

$e_g(\pi)$ orbital. In such a case, electrons are expected to be more easily injected into the d_{z^2} orbital than to the $e_g(\pi)$ orbital, when a voltage is applied. Thus the emission intensity of the π -d transition (690 nm band) is enhanced in the EL spectra. Contrary to the EL spectra, the PL and the absorption spectra directly reflect the optical transition probability. The $e_g \rightarrow d_{z^2}$ transition is a forbidden transition in the D_{4h} symmetry. Thus the electrons excited into the $e_g(\pi)$ orbital (by the Soret- or Q-band excitation) hardly fall into the d_{z^2} orbital. This explains why the 690 nm emission is absent in the PL spectra previously reported.

The EL spectroscopy is a promising technique in the study of complicated molecules such as biomolecules. This technique enables one to inject carriers directly to molecules, and to detect an optical transition that is not easily detected by ordinary spectroscopic methods. Moreover, it gives us electrical information as well as optical information.

References

- [1] P. S. Vincett, W. A. Barlow, R. A. Hann, and G. G. Roberts, *Thin Solid Films* **94**, 171 (1982).
- [2] H. Tajima, S. Ikeda, M. Matsuda, N. Hanasaki, J. Oh, and H. Akiyama, *Solid Sates Commun.* **126**, 579 (2003).
- [3] H. Tajima, S. Ikeda, K. Shimatani, M. Matsuda, Y. Ando, J. Oh, and H. Akiyama, *Synthetic Metals*, in press.
- [4] K. Shimatani, H. Tajima, T. Komino, S. Ikeda, M. Matsuda, Y. Ando, and H. Akiyama, *Chem. Lett.*, in press.
- [5] S. Ikeda, H. Tajima, M. Matsuda, Y. Ando, and H. Akiyama, *Bull. Chem. Soc. Jpn.*, in press.

Authors

H. Tajima, S. Ikeda, K. Shimatani, T. Komino, M. Matsuda, Y. Ando, and H. Akiyama

New organic superconductor, β -(*meso*-DMBEDT-TTF) $_2$ PF $_6$

Mori Group

It is of importance to investigate the electronic properties of organic (super)conductors by tuning the nanomolecular structure. Usually, the critical temperature of organic superconductor (T_c) decreases with applying pressure by -1 K/kbar. In order to apply the negative chemical pressure with the aim of the increase of T_c , the new donor molecule, *meso*-DMBEDT-TTF, by the introduction of the methyl groups to BEDT-TTF as a steric hindrance (Fig. 1) was syn-

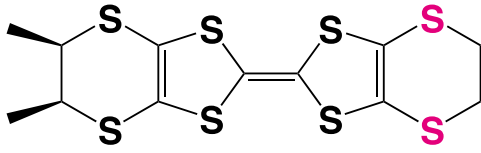


Fig. 1. Molecular structure of *meso*-DMBEDT-TTF

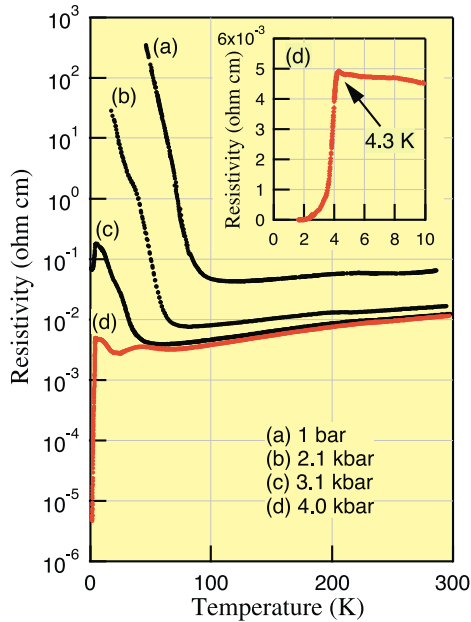


Fig. 2. The metal-insulator transition occurs at 90 K at ambient pressure. By the suppression of the transition, superconductivity is observed at $T_c = 4.3$ K under 4.0 kbar for β -(*meso*-DMBEDT-TTF) $_2$ PF $_6$.

thesized. Consequently, the new donor afforded the new organic superconductor β -(*meso*-DMBEDT-TTF) $_2$ PF $_6$ [1].

The crystal structure analysis and band calculation of β -(*meso*-DMBEDT-TTF) $_2$ PF $_6$ indicate two-dimensional dimerized structure similar to those of β -(BEDT-TTF) $_2$ X. Even though the salt has the dimerized donor arrangement, the distinct metal-insulator (MI) transition is observed at 90 K under an ambient pressure. Below 90 K, the checkerboard-type charge ordering state appears by the observation of the crystal structure analysis, confirmed by the Raman spectroscopy measurement. By applying the pressure, the MI transition is suppressed and the superconducting state was exhibited (Fig. 2). The temperature dependence of

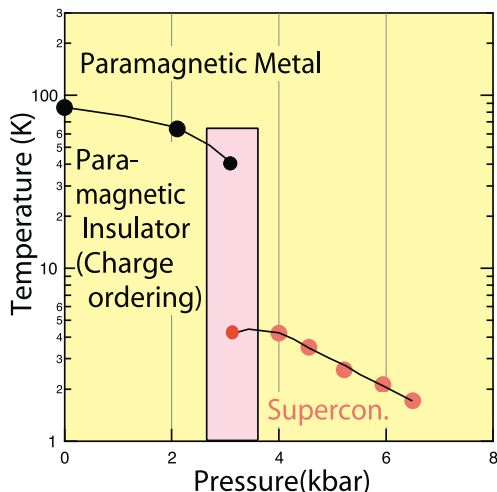


Fig. 3. Phase diagram of β -(*meso*-DMBEDT-TTF) $_2$ PF $_6$. The competition between superconducting and charge ordering states is observed in the hatched region.

magnetic susceptibility in the metallic region above 90 K follows the Heisenberg model with $J = 100$ K without the anomaly at 90 K. Even below 90 K, the susceptibility is retained and no magnetic order was observed down to 4 K. The phase diagram of β -(*meso*-DMBEDT-TTF) $_2$ PF $_6$ demonstrates the wide range of the superconducting state with $\Delta T_c / \Delta P = -0.6$ K as shown in Fig. 3.

The further study of the competition of the superconducting and charge ordering state in the hatched region (Fig. 3) is under progress.

Reference

[1] S. Kimura, T. Maejima, H. Suzuki, R. Chiba, H. Mori, T. Kawamoto, T. Mori, H. Moriyama, Y. Nishio, and K. Kajita, Chem. Commun. **21**, 2454-2455 (2004).

Authors

S. Kimura, T. Maejima, H. Suzuki, R. Chiba, T. Kawamoto^a, T. Mori^a, H. Moriyama^b, Y. Nishio^b, K. Kajita^b, and H. Mori

^aTIT

^bToho University

Theory of Fano-Kondo Effect of Transport Properties through Quantum Dots

K. Ueda Group

Recently, coexistence of the Fano effect and the Kondo effect, i.e. the Fano-Kondo effect, was experimentally observed on transport properties through T-shaped quantum dots (QDs) [1]. The line-shape of conductance was modified due to the Fano effect and became a dip in this experiment. Conductance decreases at low temperatures due to the Kondo effect when the number of electrons in QD is odd. Since this behavior is completely opposite to the usual Kondo effect, this phenomenon is called as the anti-Kondo effect. Theoretically, the Fano-Kondo effect in the T-shaped geometry studied so far [2,3,4] has been limited to the anti-Kondo case and its theoretical treatment is not general enough in contrast to the case of closed Aharonov-Bohm interferometer (AB-QD) [5].

We have investigated the Fano-Kondo effect with the tight-binding model for the T-shaped QD with an additional gate voltage V_q on the central site as shown schematically in the inset of Fig. 1. The existence of V_q is a key to realize general Fano effect in this model because the line-shape can

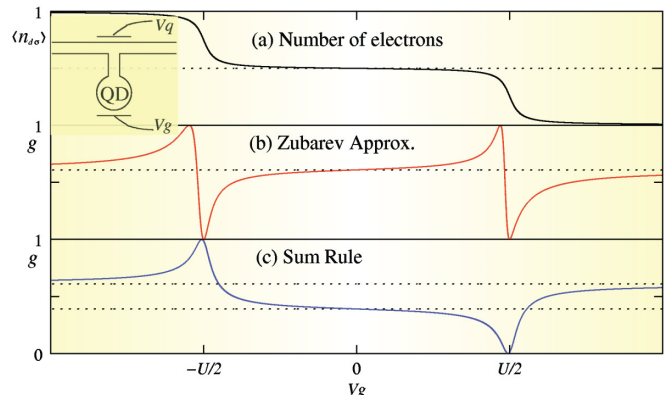


Fig. 1. (a) Number of electrons in QD as a test function of the gate voltage V_g . U on the x -axis is the Coulomb energy in the QD. (b) Conductance g in unit $2e^2/h$ obtained by Zubarev's approximation for the number of electrons defined in (a), which shows a characteristic behavior in the high-temperature regime. (c) Conductance in the low-temperature regime given by the Friedel sum rule for the number of electrons defined in (a). (Inset) Schematic figure of our model.

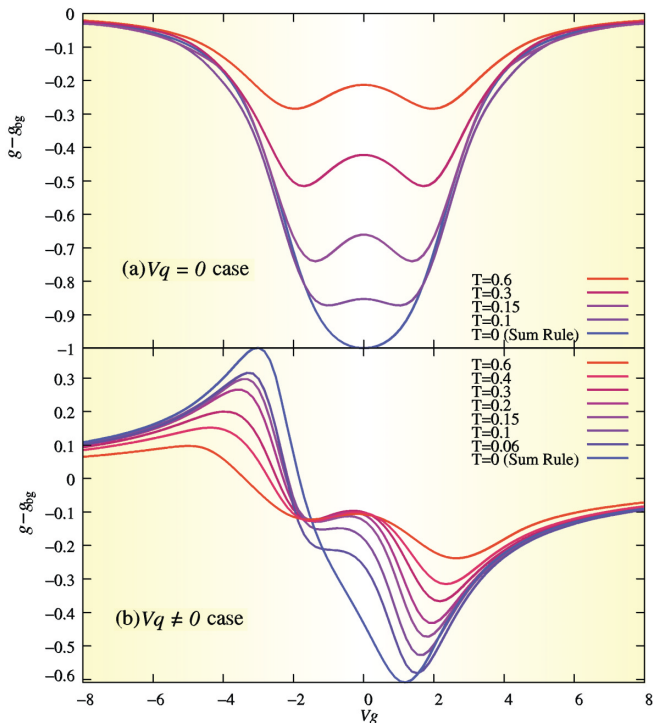


Fig. 2. Numerical results of conductance for the Coulomb interaction $U = 4$ by the FT-DMRG from a high-temperature region (red line) to a zero-temperature limit (blue line). \mathcal{G}_0 is the conductance of the background defined at $|V_g| = \infty$ limit. We note that this figure is reproduced from Fig. 6 in [6] with smoothing the points of numerical data.

be modified by V_q and in particular the conductance shows a dip structure due to the Fano effect in the $V_q = 0$ case. With this theoretical model we have shown that for a wide class of models for quantum dots there is a unified formula of conductance having a Fano asymmetric parameter. We do not write down the formula but show typical line shapes of conductance valid at high temperatures in Fig. 1 (b) and also at low temperatures in Fig. 1 (c), where it is assumed that the number of electrons at the dot sites changes as a function of the gate voltage as shown in Fig. 1 (a). With varying temperature the conductance shows a crossover between the high- and low-temperature regions compared with the Kondo temperature T_K . Behavior of the conductance at high temperatures is characterized by two Fano asymmetric line-shapes while at low temperatures by a Fano-Kondo plateau inside a Fano structure.

In order to calculate temperature dependence of the conductance explicitly we used the finite temperature density matrix renormalization group (FT-DMRG) method, by which one can calculate a thermal Green's function. The Green's function in frequency space can be obtained from the thermal Green's function by a numerical analytic continuation. The results of the numerical calculations in Fig. 2 show smooth crossover from hightemperature regime to the zero-temperature limit in (a) the anti-Kondo case by putting $V_q = 0$ and in (b) a general Fano-Kondo case ($V_q \neq 0$). Since relatively small U is used in these examples, two Fano peaks at high temperatures are not well separated from each other compared with Fig. 1. Actually, the experimental situation for the anti-Kondo effect [1] corresponds to a relatively small U , the results of which are qualitatively consistent with Fig. 2 (a). It is desired that a general Fano-Kondo effect shown in Fig. 2 (b) will be reported experimentally in near future.

References

- [1] M. Sato, H. Aikawa, K. Kobayashi, S. Katsumoto, and Y. Iye, cond-mat/0410062.
- [2] M. E. Trio, K. Hallberg, A. H. Ceccatto, and C. R. Proetto, Phys. Rev. B **65**, 085302 (2002).
- [3] K. Kang, S. Y. Cho, J. Kim, and S. Shin, Phys. Rev. B **63**, 113304 (2001).
- [4] A. Aligia and C. Proetto, Phys. Rev. B **65**, 165305 (2002).
- [5] W. Hofstetter, J. Könonig, and H. Schoeller, Phys. Rev. Lett. **87**, 156803 (2001).
- [6] I. Maruyama, N. Shibata, and K. Ueda, J. Phys. Soc. Jpn. **73**, 3239 (2004).

Authors

I. Maruyama, N. Shibata^a, and K. Ueda
^a Dept. of Basic Science, University of Tokyo

Importance of Dynamical Electron Correlation in the Stopping Power of Solids for Slow Ions

Takada Group

The concept of electron correlation permeates many subfields of condensed matter physics, but it is rather difficult to find good examples of its clear manifestation. It is even more difficult to illustrate its importance in dynamical (*i.e.*, time-dependent) processes. Here we report a success in obtaining a clean theoretical formula directly relating dynamical correlation, as characterized by f_{xc} the frequency-dependent exchange-correlation kernel of the time-dependent density-functional theory (TDDFT), with the experimentally observed stopping power, $-dE/dx$, of solids for slow ions.

The nonperturbative theory of scattering of noninteracting electrons by a central potential combined with the density-functional theory (DFT) has proved successful in calculating $-dE/dx$ of an electron gas for slow ions. This scheme accurately reproduces the measured energy loss of slow protons and antiprotons in a variety of solids. To some extent it also successfully accounts for the observed behavior in the energy loss of slow ions with increasing charge Z_1e . This kind of calculations were extended to projectile velocities v approaching the Fermi velocity of the target, but so far only few attempts have been made to include the effect of many-body dynamical correlation that is absent in the existing DFT-based schemes.

We approach the problem of including dynamical correlation in the framework of the TDDFT and have succeeded in deriving a rigorous formula for $-dE/dx$ of an interacting electron gas for ions in the limit of low projectile velocities ($v \rightarrow 0$) [1]. Depending on whether f_{xc} is involved or not, this formula can be rewritten as a sum of two terms: The first one without f_{xc} is shown to yield the conventional result for $-dE/dx$ of noninteracting Kohn-Sham electrons first reported by Echenique *et al.* [2]. The second one represents a new and important result fully incorporating the effect of dynamical correlation through the imaginary part of f_{xc} .

In the spirit of the widely used local-density approximation (LDA), we can think of an appropriate approximation to f_{xc} in such a form as the one proposed by Qian and Vignale [3]. Then our formula enables us to make a reasonably accurate evaluation of the friction coefficient ($-dE/dx$ divided by v in the limit of $v \rightarrow 0$) of an interacting electron gas as a function of the atomic number of the projectile ion Z_1 . An example of the results obtained by such calculations for the homogeneous electron gas is shown in Fig. 1 in which the

Novel Low-Field Magnetoresistance Oscillation Effect in Short Period Unidirectional Lateral Superlattices

Iye Group

Electron dynamics in a periodic potential is at the heart of solid state physics. For the experimental exploration of various model cases, high mobility two-dimensional electron gas (2DEG) in a GaAs/AlGaAs device with an appropriately microfabricated superstructure is most suitable. In such a system, electrons move ballistically in an artificial potential landscape with minimal influence from disorder potential. Application of perpendicular magnetic field adds an extra ingredient to the electron dynamics.

A typical example, which is also the situation for the present study, is a unidirectional lateral superlattice, where 2D electrons are subjected to a one-dimensional periodic modulation of potential. For this system, two characteristic magnetotransport features have been elucidated: One is the so-called commensurability oscillation (CO) effect, and the other is the positive magnetoresistance (PMR) effect. The former arises from commensurability, or geometrical resonance, between the cyclotron radius $R_c = \hbar k_F / eB$ and the modulation period a . The latter is associated with the so-called snake orbit. These effects are basically understood within a semiclassical magnetotransport picture and do not explicitly require miniband formation. In the present study, we have observed a novel oscillatory magnetoresistance effect which is attributed to geometrical resonance of open orbits created by miniband formation.

The structure of the sample is schematically shown on the top panel of Fig.1. A comb-like pattern of resist on the surface of the GaAs/AlGaAs device creates a weak unidirectional potential modulation at the 2DEG plane with period ranging from 138 to 184 nm. The amplitude of the potential modulation is typically 0.01 to 0.03 of the Fermi energy E_F of the 2DEG.

The main panel of Fig.1 shows the magnetoresistance

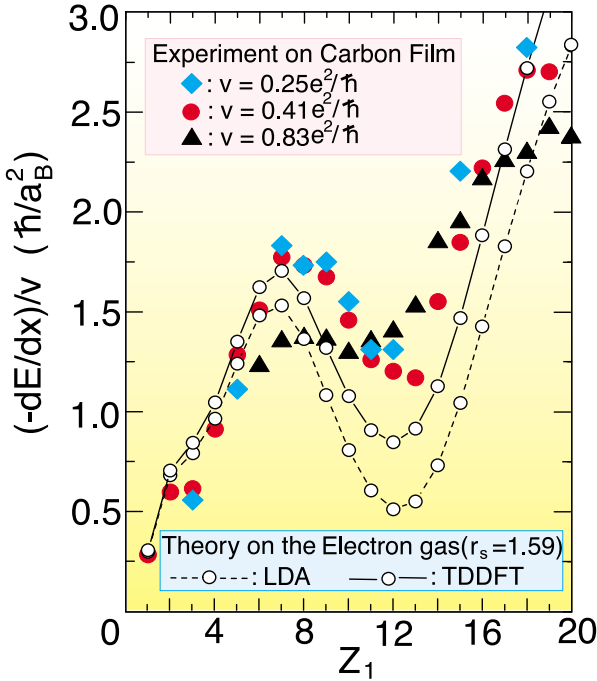


Fig. 1. Comparison between experiment on the stopping power, $-dE/dx$, of carbon films for slow ions (characterized by the atomic number Z_1) with three different values of the velocities v and theory on the same quantity of the homogeneous electron gas with the electron density equivalent to the valence-electron density in carbon in the limit of zero ion velocity ($v \rightarrow 0$).

solid and dashed curves correspond, respectively, to the cases with and without dynamical correlation (or the second term in our formula). Here the electron density characterized by the conventional density parameter r_s is taken to be 1.59 which is just the same density as the one for valence electrons in carbon films. In view of the fact that at low velocities the energy loss of ions in solids is due mainly to the stopping power of valence electrons, our present theoretical results can be directly compared with the experimental ones in carbon.

As can be seen in Fig. 1, experiment exhibits an oscillatory behavior in the friction coefficient with increasing Z_1 . This behavior, which is attributed to the shell structure of valence electrons around the ion, is reproduced rather well in the DFT-based calculation (as labeled by LDA), but a better quantitative agreement with experiment is obtained by our theory based on the TDDFT, thanks to the enhancement of $-dE/dx$ by dynamical correlation, or more specifically, the excitonic effect which has recently been revealed to be very prominent through the accurate calculation of the dynamical structure factor of the homogeneous electron gas [4].

Agreement between theory and experiment becomes unsatisfactory for Z_1 larger than about 20, indicating a need to go beyond the LDA-type approximation in the description of f_{xc} .

References

- [1] V. U. Nazarov, J. M. Pitarke, C. S. Kim, and Y. Takada, Phys. Rev. B **71**, 121106(R) (2005).
- [2] P. M. Echenique, R. M. Nieminen, and R. H. Ritchie, Solid State Commun. **37**, 779 (1981).
- [3] Z. Qian and G. Vignale, Phys. Rev. B **65**, 235121 (2002).
- [4] Y. Takada and H. Yasuhara, Phys. Rev. Lett. **89**, 216402 (2002).

Authors

V. U. Nazarov^a, J. M. Pitarke^b, C. S. Kim^a, and Y. Takada^a
^a Chonnam National University
^b Euskal Herriko Unibertsitatea

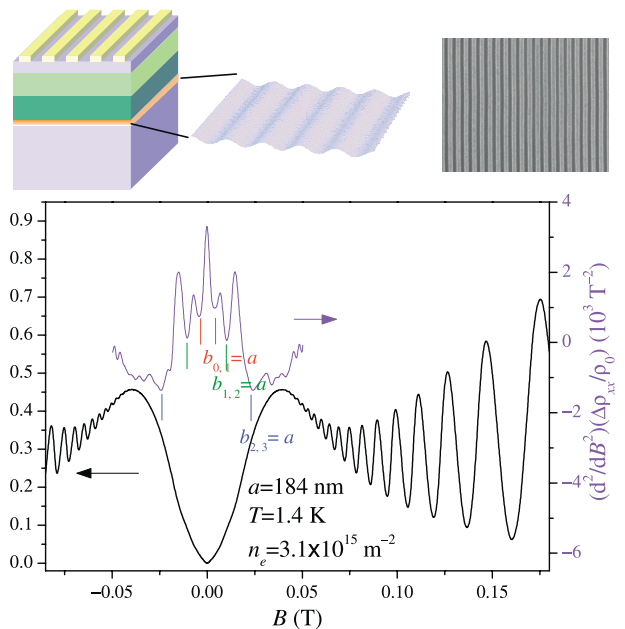


Fig. 1. Top panel: schematic drawing of the structure and an SEM picture of the sample. Main panel: Magnetoresistance trace in the low field range showing the PMR and CO features. Small amplitude oscillation seen in the PMR region is made conspicuous in the second derivative trace.

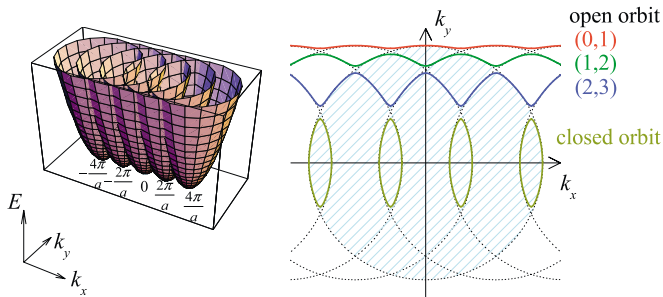


Fig. 2. Left panel: Energy bands of 2DEG reconstructed by the superlattice potential. Right panel: Open orbits created by the Bragg reflection. The corresponding trajectories in real space are isomorphic to these but rotated by 90 degrees.

trace in the low field range. The two characteristic features mentioned above, *i.e.* PMR and CO, are prominent. We have found that a small amplitude oscillation is superposed on the trace in the PMR region. The oscillation can be made conspicuous by taking the second derivative of the trace, which is shown in the same figure. The oscillation gradually dies away at higher temperatures.

In Fig.2, the energy bands of 2DEG reconstructed in the presence of periodic potential and the open orbits thereby are shown. The electron trajectories in real space are isomorphic to these except they are rotated by 90 degrees. The widths of these wiggling trajectories in real space, which we denote by $b_{i,j}$ for the trajectory (i, j) , can be calculated from an elementary geometry as

$$b_{i,j} = \frac{\hbar k_F}{e|B|} \left[\sqrt{1 - \left(\frac{i\pi}{ak_F}\right)^2} - \sqrt{1 - \left(\frac{j\pi}{ak_F}\right)^2} \right] \quad (1)$$

Geometrical resonance occurs when one of the $b_{i,j}$'s coincides with integer multiples of a . The calculated values of the magnetic field show excellent agreement with the observed positions of resistance maxima. Their changes with the electron density and the modulation period are also consistently explained by the model, rendering a strong support.

It is stressed that the newly observed oscillatory magnetoresistance effect, which is attributed to geometrical resonance of the open orbit trajectory and the superlattice periodicity, is a manifestation of the miniband formation.

Reference

- [1] A. Endo and Y. Iye, Phys. Rev. B **71**, 081303(R) (2005).

Authors

A. Endo and Y. Iye

The Kondo Effect Recovers Quantum Coherence

Katsumoto Group

It is well known that quantum coherence of an electron traversing in the vacuum or a metal is lost when it is "observed". The observation process can be viewed as formation of entanglement with "environment" of infinite numbers of freedom. Such a process can be triggered by various origins, *e.g.*, spin-scattering with local magnetic impurities. We have confirmed that by observing an amplitude of Aharonov-Bohm (AB) oscillation in a ring with a quantum dot, which can work as a magnetic impurity[1].

At the same time, however, the spin-scattering is the elementary process to form a Kondo state, which is in reso-

nance with the Fermi energy when the local spin is 1/2. The Kondo state should thus be a coherent state though it is an entanglement of huge number of freedoms.

The best way to check this property is to see the quantum interference of a Kondo state. For this purpose, we have adopted a quantum wire with a side-coupled quantum dot, which is schematically shown in the inset of Fig.1. Here the interference occurs between the direct path and the path with a bounce to the quantum dot. The potential of the dot can be varied with the gate voltage V_g and the coupling strength can also be tuned by the voltage V_m .

In this structure ordinal Coulomb peaks of the conductance trough the dot versus gate voltage appear as dips in the conductance through the wire due to the interference. This is a kind of the Fano effect [2] and the lineshape shown in the topmost of Fig.1 really has Fano distortion. With increasing the coupling strength, the conductance between two adjacent dips decreases alternatively as marked A and B. At last neighboring dips are combined into single dips. This is a clear sign of the Kondo resonance. We have thus observed the Fano-Kondo effect.

From the observation we can clearly say that the Kondo state is quantum mechanically coherent. An interesting observation is that the direction of the distortion in the lineshape rapidly changes with the growth of the Kondo state (in the case of dip A, around cyan-colored curve). This is due to the enhancement of coupling strength from asymptotic strong coupling nature of the Kondo effect.

References

- [1] H. Aikawa, K. Kobayashi, A. Sano, S. Katsumoto, and Y. Iye, Phys. Rev. Lett. **92**, 176802 (2004).
 [2] K. Kobayashi, H. Aikawa, S. Katsumoto, and Y. Iye, Phys. Rev. Lett. **88**, 256806 (2002).

Authors

S. Katsumoto, M. Sato, H. Aikawa, and Y. Iye

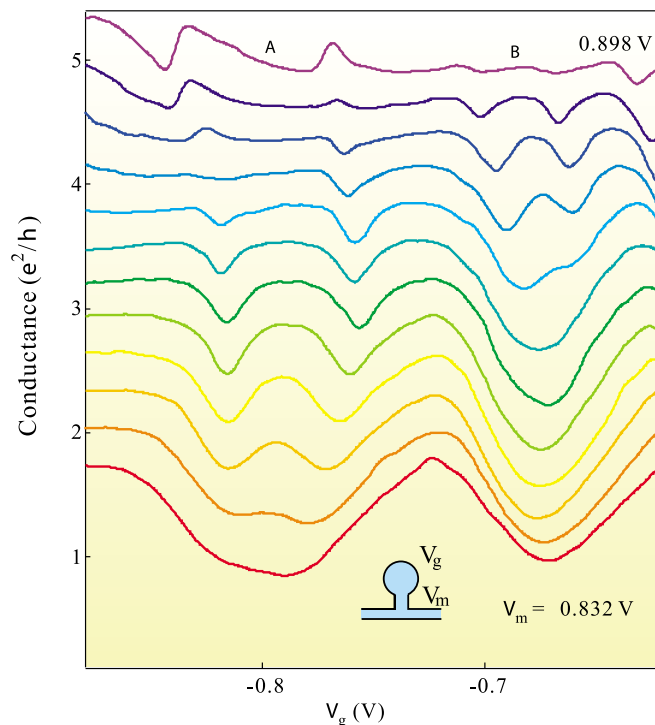


Fig. 1. Conductance of the wire versus the gate voltage V_g of the side-coupled dot measured at several coupling strength tuned by the coupling gate voltage V_m . The step in V_m is 6mV and the data are offset by $0.3e^2/h$ for clarity. The inset shows a schematic diagram of the sample.

Direct Observation of Strain-Induced Change in Surface Electronic Structure on the Cu(001) Surface

Komori Group

Recent experimental studies have reported that chemical reactions on d-electron metal surfaces can be modified by the external strain [1]. Theoretical attempts to interpret these phenomena have been done on the basis of first-principles calculations of electronic structure, whereas there have been little experimental efforts to examine the electronic structure itself. We have adopted the Cu(001) surface as a model system, whose "natural" electronic structure is well-known, and demonstrated [2] the direct evidence of the strain-induced change of individual Cu3d states by angle-resolved photoemission spectroscopy.

We introduced a local strain field on the Cu(001) surface by nitrogen partial adsorption. At 0.3 mono-layer (ML) of the averaged nitrogen coverage, the surface is covered with a well-ordered array of the N-adsorbed domain as shown in

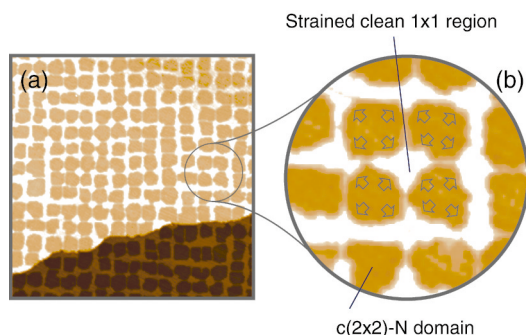


Fig. 1. (a) STM image of the partially nitrogen-adsorbed Cu(001) surface. The Dark area is the N-adsorbed domain, and the bright part corresponds to the remaining clean region. The nitrogen coverage is 0.3 ML, and the image size is 100 nm \times 100 nm. (b) Magnification of the STM image. The arrows schematically indicate the direction of atom replacement in the N-adsorbed domain. The clean surface is thus compressed.

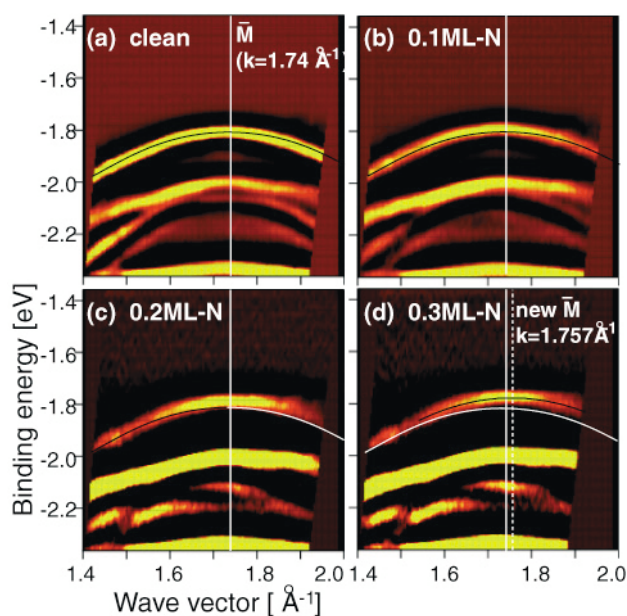


Fig. 2. Band dispersions experimentally observed on the clean (a), 0.1 ML N-adsorbed (b), 0.2 ML (c) and 0.3 ML (d) surfaces. The solid curves in (a-c) and the white curves in (c,d) indicates the band dispersion of the Tamm state, a surface state, determined on the clean surface. The solid curve in (d) show the Tamm state band dispersion. The white line in each figure represents the folding point of the Tamm state on the clean surface, and the white dotted line in (d) shows the new folding point. Both the energy at M and the wave vector of the folding point shift with increasing the N-coverage.

Fig. 1. The clean Cu region imaged brightly is compressed because of the large lattice constant on the N-adsorbed domain. In a simple approximation, the Cu lattice deformation on average will be proportional to the nitrogen coverage.

Figure 2 shows the observed band dispersions around the M point on the clean, 0.1 ML, 0.2 ML and 0.3 ML nitrogen-adsorbed surfaces. In these figures, we can see two kinds of electronic structure change: (1) the binding energy of the Tamm state decreases with increasing the nitrogen coverage, i.e., the increase of the strain at the clean region, (2) the folding point of the Tamm state moves to a larger k-point with increasing the strain.

The experimental results were compared with the first-principles calculations with a symmetric slab model. A uniform compressive stress was given to the slabs laterally while interlayer relaxation due to the stress was allowed for the simulation of the strained Cu surface. The calculated energy shifts of the surface states excellently agree with the observation. Moreover, the shift of the folding point of the Tamm state is quantitatively explained by the sum of the Brillouin zone extension and the change of the work function due to the lattice constant reduction.

References

- [1] For example, M. Gsell *et al.*, Science **280**, 717 (1998).
- [2] D. Sekiba, *et al.*, Phys. Rev. Lett. **94**, 016808 (2005).

Authors

D. Sekiba, K. Nakatsuji, Y. Yoshimoto, and F. Komori

Direct Observation of a Precursor State for Chemisorption: Ethylene on Si(100)c(4 \times 2)

Yoshinobu Group

The cycloaddition reaction of alkene to the Si(100) surface is one of the promising methods to link an organic molecule to the substrate via stable di- σ SiC bonds. Since the discovery of the di- σ bonded ethylene on Si(100), many experimental and theoretical studies have been reported on the chemisorbed state. In addition, the reaction mechanism has been challenged because the frontier orbital theory requests that the [2+2] cycloaddition reaction between ethylene and the symmetric dimer on Si(100) is apparently forbidden in thermal reaction. However, only a few studies have been reported on the reaction mechanism of di- σ bond formation. In this study, we report the direct observation of a precursor state for the di- σ bond formation of ethylene on Si(100)c(4 \times 2) using high-resolution electron energy loss spectroscopy (HREELS) at low temperature, and the stable precursor state is identified as a weakly adsorbed π -complex type for the first time.

In Figure 1, EELS spectra at 48 K show several new peaks in addition to the vibrational peaks originating from the di- σ ethylene species. Judging from the CH stretching (3051 cm^{-1}) and the CC stretching (1522 cm^{-1}) modes and the strong CH₂ wagging mode at 968 cm^{-1} , these peaks originate from a weakly adsorbed ethylene species. By comparing the vibrational spectra of chemisorbed ethylene with ethylene-transition metal complex, we conclude that this weakly adsorbed ethylene is a π -complex type. Using the empirical relation between the CC stretching energy and the CC bond length for adsorbed ethylene species, the CC bond length of this species is estimated to be 1.38 Å.

Development of Novel Probes for Atomic Force Microscopy

Hasegawa Group

Atomic force microscopy (AFM) has been utilized to image nano-scale surface topograph including its atomic structure through a detection of forces on the surface. How to detect the force, thus, plays a crucial role in spatial resolution and detection efficiency of AFM. Here we reports two new AFM probes which show unique performances.

In usual AFM operations, a commercial cantilever with a tip made of Si is used as a force sensor. In some cases, however, such as magnetic force microscopy and scanning capacitance microscopy, a metal probe is desired because of its high conductivity and magnetic properties. Most of the metal probes are produced by coating, making the tip blunt and deteriorating the spatial resolution. In order to avoid the dull tip without losing a high Q factor of the Si cantilever, we formed a metal-tip cantilever by attaching a 5 μ m-diameter tungsten tip to the commercial Si cantilever and sharpening it with focused ion beam (FIB) [1]. TEM observation revealed that the curvature radius of the W tip is quite small, *ca.* 3.5nm.

Atomically resolved non-contact (nc) AFM image of the Si(111)-(7 \times 7) surface was successfully taken with the tip. This micro-fabrication method is applicable to any conductive wires. So far, we have made a Au-tip cantilever and succeeded in drawing a line of Au with a width of *ca.* 100nm on a Si substrate by field evaporation from the tip.

In nc-AFM, small oscillation amplitude is desirable for a detection of short-range forces, which contributes to the atomic resolution [2]. The small oscillation amplitude using a conventional cantilever, however, causes a snapping of the cantilever into the sample ("jump to contact"). To avoid the tip crash we need to use a sensor with a high stiffness. We thus developed an AFM probe using a quartz length-extension resonator (LER) whose spring constant is quite high (~540 000 N/m) (Fig. 2(a)). Self-sensing capability of quartz due to its piezoelectric effect eliminate a need of using cumbersome optical alignments, preferable for low temperature applications.

A tungsten tip was attached on the LER rod (Fig. 2(b)), and was fabricated with FIB as a tip [3] (Fig. 2(c)). Prior to the AFM experiment, field ion microscopy observation of the tip was performed *in-situ* to remove the oxide layer. Atomically resolved nc-AFM imaging of the Si(111)-7 \times 7 surface was obtained with the probe (Fig. 2(d)), demonstrating

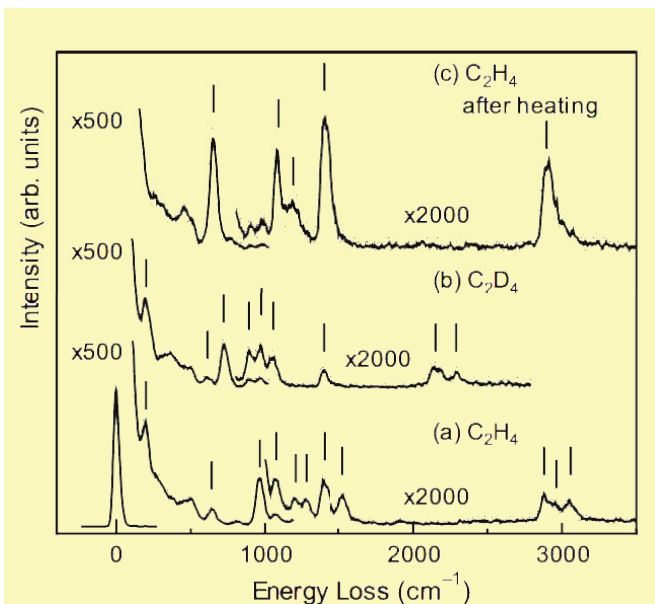


Fig. 1. HREELS spectra of (a) C₂H₄ and (b) C₂D₄ on Si(100)c(4 \times 2) at 48 K. (c) After exposing C₂H₄ on Si(100) at 48 K followed by heating at 150 K, the spectrum was measured at 48 K. All spectra were measured in the specular mode. The primary electron energy, $E_p=5.0$ eV.

When the Si surface exposed to ethylene at 48 K was annealed at 150 K, the peaks originating from the π -complex species disappeared and the peaks originating from the di- σ bond species were increased in intensity. Therefore, the adsorbed π -complex species is a precursor state for the di- σ chemisorption. It should be noted that the π -complex precursor and the di- σ species coexist at low temperature, and the reaction from the precursor to the di- σ species does not proceed at 48 K. This suggests that when gaseous ethylene molecules enter the adsorption potential on Si(100)c(4 \times 2) some molecules are trapped in the intrinsic precursor state, but the other molecules can proceed to the di- σ bond formation. From the vibrational spectra as a function of temperature, the activation energy E_a is roughly estimated to be 0.2 eV using the Arrhenius formula (see Fig.2).

Reference

[1] M. Nagao, H. Umeyama, K. Mukai, Y. Yamashita, J. Yoshinobu, K. Akagi, and S. Tsuneyuki, J. Am. Chem. Soc. **126**, 9922-9923 (2004).

Authors

M. Nagao, H. Umeyama, K. Mukai, Y. Yamashita, J. Yoshinobu, K. Akagi^a, and S. Tsuneyuki^a

^aDepartment of Physics, University of Tokyo

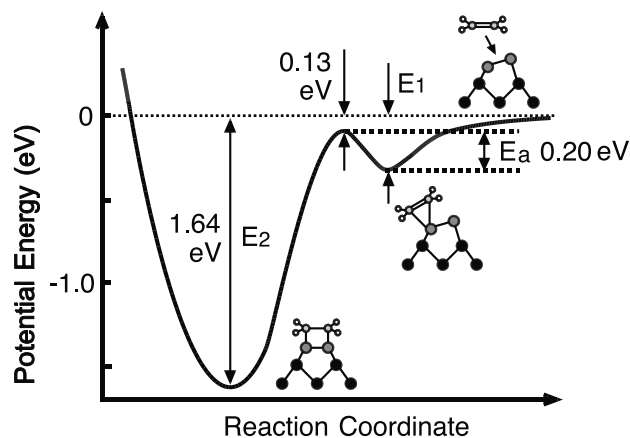


Fig. 2. Potential energy diagram for the chemisorption of ethylene on Si(100)c(4 \times 2). E_a , E_1 and E_2 represent the activation energy for the di- σ formation, the adsorption energy of the precursor state and that of the di- σ chemisorption state, respectively.

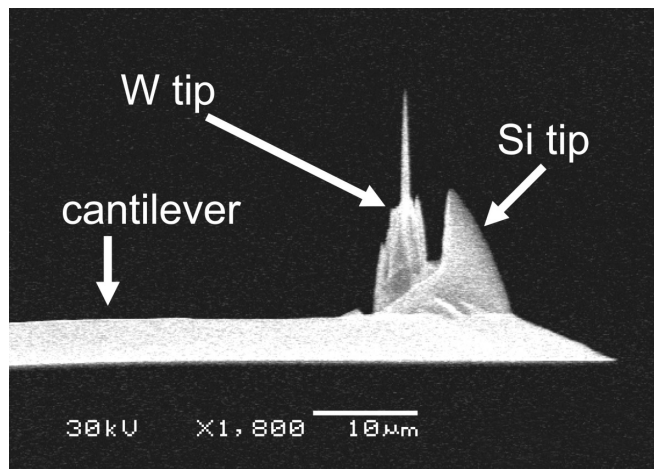


Fig. 3. SEM image of the W tip attached to the Si cantilever

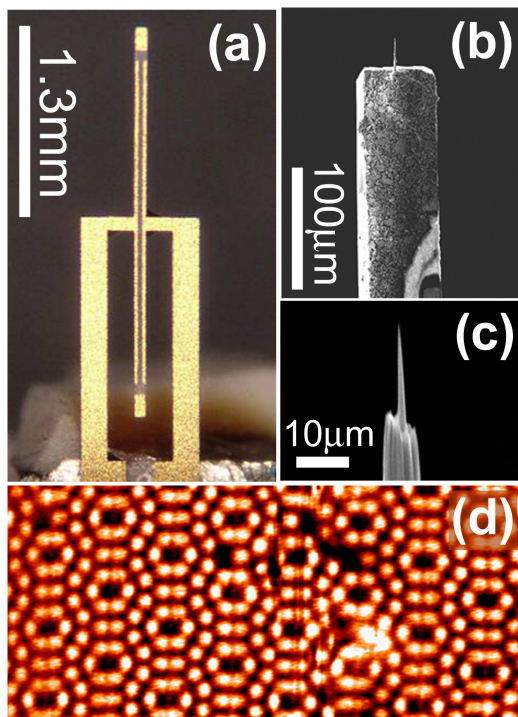


Fig. 2. (a) a quartz LER (b) a SEM image of the front rod with a W tip. (c) a zoomed SEM image of the W tip fabricated by FIB. (d) an nc-AFM image of the Si(111)-7×7 surface. The observed area is 19 nm × 9 nm.

its high performance.

The TEM and SEM observations and the FIB processing were performed at Electron Microscope Section of Materials Design and Characterization Laboratory in ISSP. Technical assistance by M. Ichihara and F. Sakai is highly appreciated.

References

- [1] K. Akiyama, T. Eguchi, T. An, Y. Fujikawa, Y. Tamada-Takamura, T. Sakurai, and Y. Hasegawa, *Rev. Sci. Instrum.* **76**, 033705 (2005).
- [2] T. Eguchi and Y. Hasegawa, *Phys. Rev. Lett.* **89**, 256105 (2002).
- [3] T. An, T. Eguchi, K. Akiyama, and Y. Hasegawa, to be published in *Appl. Phys. Lett.*

Authors

K. Akiyama, T. An, T. Eguchi, M. Hamada, and Y. Hasegawa

Metallic Heteroepitaxial Oxide Nanowire Arrays

Lippmaa Group

Transition metal oxides are well known for a wide variety of ordering mechanisms and rich electronic phase diagrams. Our work is focused on understanding the electronic structure and properties of oxides in confined geometries, such as two-dimensional layers, nanowires, or nanodots. In this work we have studied the transport properties of LaTiO₃ nanowire arrays embedded in SrTiO₃. A typical layer thickness for LaTiO₃ is one unit cell, while the width of the wire is in the 20 to 50 nm range, as shown in Fig. 1.

LaTiO₃, in its stoichiometric form, is a Mott insulator. Metallic conductivity, however, can be easily induced by slight doping. In our case, since the single unit cell-thick LaTiO₃ films are grown on Sr-terminated SrTiO₃ substrates and embedded in SrTiO₃, it is more accurate to look at the films as consisting of (La,Sr)TiO₃, where the actual carrier concentration in the LaTiO₃ layer depends on charge transfer

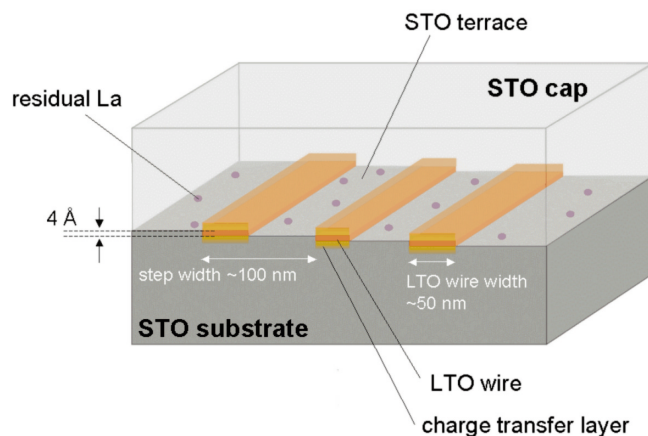


Fig. 1. Model of a LaTiO₃ nanowire array embedded in SrTiO₃. The wire layer has a thickness of one unit cell.

effects between the film and the surrounding SrTiO₃. The electronic thickness of the wires is therefore larger than the physical thickness.

The nanowires were grown by pulsed laser ablation at a temperature of 1000°C in step-flow mode by depositing approximately half a monolayer of LaTiO₃. In this growth mode the newly-deposited material decorates the step edges of a vicinal substrate surface. The density of wires can thus be adjusted by changing the miscut angle of the substrate.

We found that wires and thin LaTiO₃ layers on an open substrate surface become insulating, likely because of the formation of depletion layers due to the presence of surface states. The nanowire arrays were therefore capped with a 10 nm-thick SrTiO₃ layer. Contact to the wires was made by bonding wires directly to the crystal surface, penetrating the thin capping layer (Fig. 2,top).

The low-temperature resistivities measured along the direction of the wires and perpendicular to the wires are shown in Fig. 2. Due to the relatively large contact area of the wire bonding pads, these measurements reflect the properties of approximately 100 wires connected in parallel. As shown in Fig. 2, the temperature dependence of resistivity

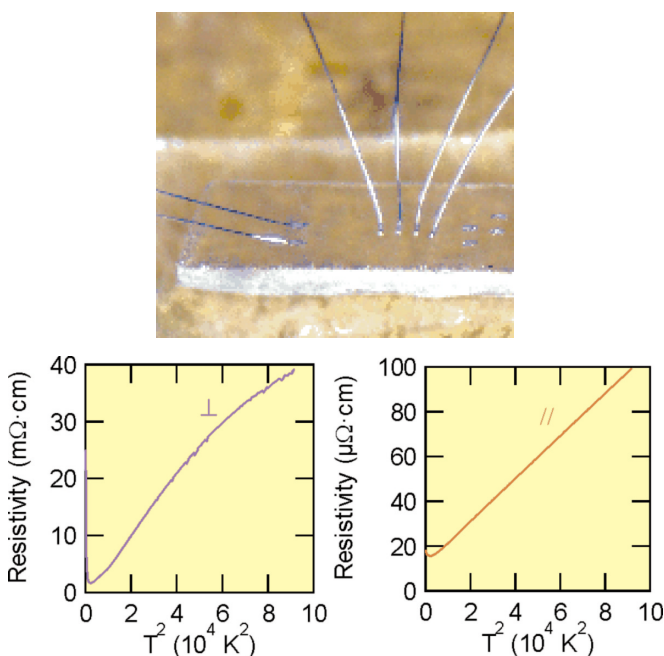


Fig. 2. (Top) a photo of a transparent metallic nanowire array. The wire direction is vertical in the image. Bonding wires used for transport measurements are visible on the crystal surface. (Bottom) Low-temperature transport measurements of a wire array perpendicular (⊥) and parallel (∥) to the wire direction.

along the wires on a T^2 scale is very close to linear, as expected for doped (La,Sr)TiO_{3+δ} for a carrier concentration of $\approx 10^{22}$ cm⁻³. In contrast, the resistivity along the perpendicular direction is nearly three orders of magnitude higher and shows a nonlinear behavior on a T^2 scale. This behavior and resistivity values are characteristic of lightly-doped SrTiO₃, with a carrier concentration in the 10^{19} cm⁻³ range. Note that carrier localization appears to occur in this direction at temperatures below about 50 K.

The wire array has a very regular structure and we have confirmed wire conductivity over a distance of several millimeters. The uniformity of the wire array depends mainly on the quality of the substrate polishing, since the wires follow the surface steps without breaking.

Reference

[1] T. Mihara, K. Shibuya, T. Ohnishi, H. Koinuma, and M. Lippmaa, *Thin Solid Films*, in print.

Authors

M. Lippmaa, T. Ohnishi, T. Mihara, and K. Shibuya

Successive Transitions in Charge Density Wave State under High Magnetic Fields

Osada group

We have studied possible phase diagram of charge density wave (CDW) state under magnetic fields by analyzing the density response function, and successfully explained mysterious successive transitions observed in high-field CDW state in organic conductors α -(BEDT-TTF)₂KHg(SCN)₄ and (Per)₂M(mnt)₂ (M=Au, Pt).

Generally, the zero-field insulating CDW phase (CDW₀) is destabilized due to Zeeman effect in sufficiently strong magnetic fields. In higher magnetic fields and sufficiently low temperatures, there appears a new metallic CDW phase (CDW_x) where only one spin-subband contributes to density wave formation. The high-field "kink transition" in α -(BEDT-TTF)₂KHg(SCN)₄ is considered as CDW₀-CDW_x transition. In this compound, however, irregular successive

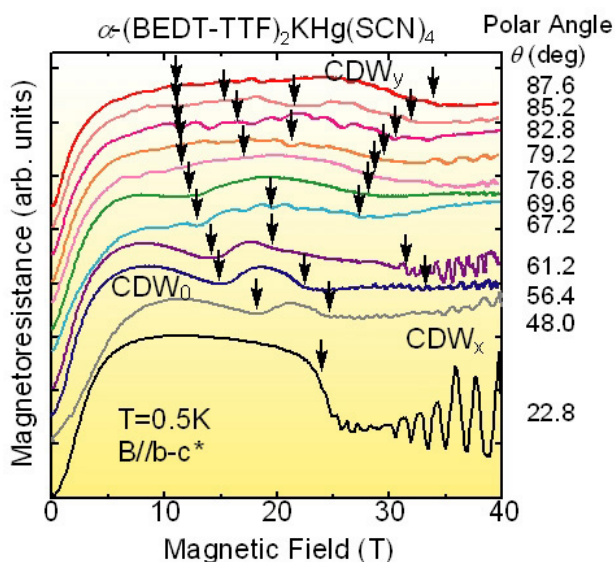


Fig. 1. Interlayer magnetoresistance of an organic conductor α -(BEDT-TTF)₂KHg(SCN)₄ for different field orientations measured by the polar angle θ from the normal of 2D plane. As indicated by arrows, several transitions appear between the low-field CDW phase (CDW₀) and the high-field one (CDW_x) under tilted magnetic fields.

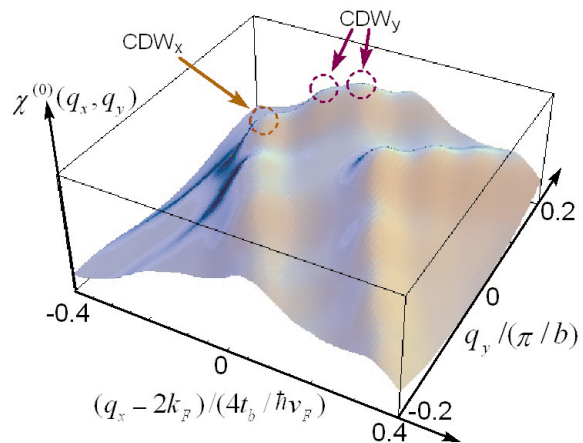


Fig. 2. Wave-number dependence of the density response function of highly anisotropic 2D electron system under magnetic fields. Peaks indicated by arrows correspond to possible CDW channels. Nesting imperfection could stabilize semimetallic CDW_y subphases which cause successive transitions between CDW₀ and CDW_x.

phase transitions have recently been discovered between CDW₀ and CDW_x phases under tilted magnetic fields [D. Andres *et al.*, PRB68, 201101 (2003)]. We have confirmed these phenomena in wider field range using 50T-class non-destructive pulsed high magnetic fields as shown in Fig.1. The successive transitions extend over the wide field range from 12T to 40T, which is hardly explained by the quantized changes of the CDW wave number in CDW₀-CDW_x transition as suggested by Andres *et al.*

In order to clarify the origin of the successive phase transitions, we have investigated the CDW instability of highly anisotropic two-dimensional electron systems by evaluating the density response function under magnetic fields. We have found that nesting imperfection of two Fermi sheets could stabilize semimetallic CDW state (CDW_y) in higher field region of CDW₀ even in the systems without any CDW-SDW mixing as assumed by Zanchi *et al.* [PRB53, 1240 (1996)]. In the CDW_y state, both up-spin and down-spin subbands show imperfect nesting leaving electron and hole pockets, respectively. Moreover, the CDW_y state could be divided into subphases at low temperatures resulting from the quantized nesting effect in the similar manner as the field-induced SDW case. In each subphase, one of electron and hole pockets is fully quantized by breaking electron-hole compensation. It causes finite Hall effect. After successive transitions among the CDW_y subphases, finally, the system undergoes the transition into a metallic CDW_x state.

The above picture well explains the phase transitions observed in α -(BEDT-TTF)₂KHg(SCN)₄, and it might be also applicable to the successive field-induced CDW transitions in (Per)₂M(mnt)₂ (M=Au, Pt).

Authors

T. Osada, E. Ohmichi, M. Kobayakawa, A. Ogasawara, K. Kajiki, and H. Imamura

Pressure Induced Metal-Insulator Transition in CeRu₄Sb₁₂ Single Crystal

Uwatoko Group

Ternary intermetallic compounds RT₄X₁₂ (R=rare earth; T=Fe, Ru, Os; X=P, As, Sb) with the skutterudite structure have various physical properties [1]. Among them, most of

the Ce-based compounds $\text{CeT}_4\text{X}_{12}$ show semiconductive behavior which might be attributed to the large c - f hybridization strength originated from the unique structure. Actually, magnitude of energy gap increases with decreasing lattice constant in $\text{CeT}_4\text{X}_{12}$ [2]. $\text{CeRu}_4\text{Sb}_{12}$ is, exceptionally, metallic not explained by the band calculation which predicts it semiconducting. Moreover, $\text{CeRu}_4\text{Sb}_{12}$ shows anomalous behaviors such as heavy fermion and non-Fermi-liquid(NFL) [3,4] at ambient pressure. Recently, Kobayashi et al. reported NFL behavior is suppressed with an extension of Fermi liquid regime under $P=1.3$ GPa [4]. These features must be related to the delicate electronic structure in the vicinity of the Fermi level. This is supported by Shubnikov-de Haas and the de Haas-van Alphen experiments in $\text{CeRu}_4\text{Sb}_{12}$ which clarified small Fermi surface at low temperature with highly enhanced effective mass [5]. It is expected that c - f hybridization plays important roles in the electrical mechanism of $\text{CeRu}_4\text{Sb}_{12}$. Therefore, we have studied the transport properties under applied high pressure which can have a profound effect on the c - f hybridization.

Figure 1 shows a temperature dependence of the electrical resistivity of $\text{CeRu}_4\text{Sb}_{12}$ under several constant pressures, 1.5 - 8 GPa, respectively. In order to obtain the magnitude of the energy gap at low temperature, we assume $\text{CeRu}_4\text{Sb}_{12}$ being simple activated semiconductor and plot $\ln\rho$ as a function of $1/T$. A linear relation is observed in a narrow and limited temperature range. Fits to an activated conduction law

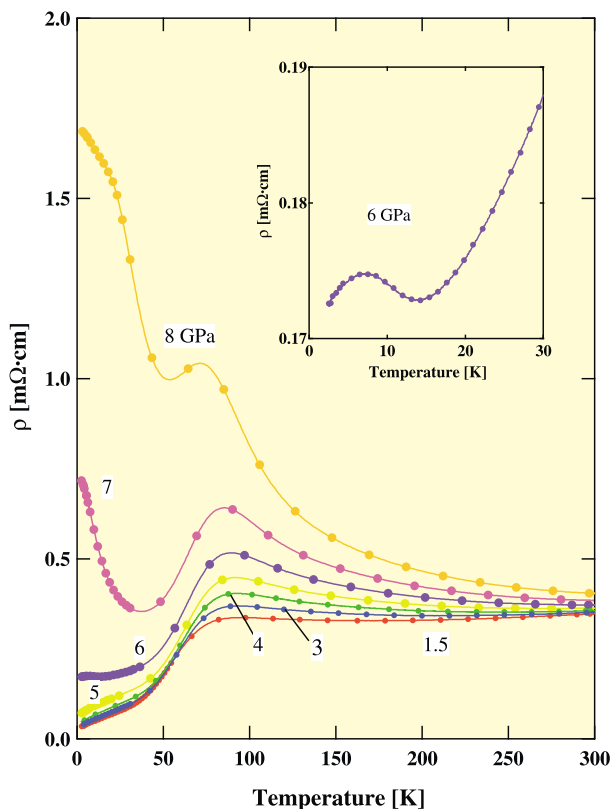


Fig. 1. Temperature dependence of electrical resistivity in $\text{CeRu}_4\text{Sb}_{12}$ under several constant pressures, 1.5-8 GPa. The inset in figure 1 shows the resistivity at low temperature under 6 GPa. At 1.5 GPa, the resistivity exhibits a maximum (ρ_{\max}) around 80 K (T_{\max}) above which it shows $-\log T$ dependence due to Kondo scattering, based on the same mechanism at ambient pressure. Below 80 K it decreases rapidly. The resistivity has small pressure dependence, up to 5 GPa, except that ρ_{\max} tends to be gradually remarkable with increasing pressure. As shown in Fig.1 inset, the resistivity under 6 GPa has a small maximum around 8 K. With further increasing pressures, the resistivity is enhanced as a whole and drastically at the low temperature regime. Semiconducting behavior was stabilized under high pressure in $\text{CeRu}_4\text{Sb}_{12}$. While, the resistivity at 8 GPa shows a tendency to saturate with decreasing temperature.

$\rho = \exp(\Delta/T)$ yield small band gap $\Delta = 0.3$ K, 9.1K, 24.7 K under $P = 6$ GPa, 7 GPa, 8 GPa, respectively. A pressure coefficient of the energy gap $d\Delta/dP$ is about 12.2 K/GPa. The magnitude of Δ under high pressure is close to that of $\text{CeOs}_4\text{Sb}_{12}$, $\Delta \sim 10$ K[6]. This is consistent with the relationship between Δ and a lattice constant in $\text{CeT}_4\text{X}_{12}$ as mentioned at the beginning. The problem is that T_{\max} is slightly shifted to lower temperature side as increasing pressures. This fact is contrary to effect of pressure on the typical Ce-based Kondo compounds, though no clear explanation has been made. Investigation of the physical properties under higher pressure can lead us to solving them. The electrical mechanism of $\text{CeRu}_4\text{Sb}_{12}$ being small band-gap semiconductor under high pressure may have the same origin as other Ce-based skutterudite compounds which show semiconducting behaviors. More researches, such as Hall Effect measurement under high pressure, are necessary to understand the electrical mechanism of $\text{CeRu}_4\text{Sb}_{12}$ more precisely and are in progress.

References

- [1] H. Sato *et al.*, Phys. Rev. B **62**, 15125 (2000)
- [2] I. Shirovani *et al.*, J. Solid State Chem. **142**, 146 (1999)
- [3] N. Takeda *et al.*, J. Phys. Conds. Matter. **13**, 5971 (2001).
- [4] M. Kobayashi *et al.*, Physica B **329-333**, 605 (2003).
- [5] K. Abe *et al.*, Physica B **312-313**, 256 (2002).
- [6] E.D. Bauer *et al.*, J. Phys. Cond. Matter **13**, 4495 (2001)

Authors

N. Kurita, M. Hedo, Y. Uwatoko, M. Kobayashi^a, H. Sugawara^a, and H. Sato^a
^aTokyo Metropolitan University

Nonlinear Optics in the Extreme Ultraviolet

Watanabe Group

Attosecond pulse generation was realized through high harmonic generation and has made it possible to observe attosecond phenomena [1]. Another interesting application of attosecond pulses is nonlinear optics in the XUV and soft x-ray regions, demanding the spatial and temporal coherence of light sources. So nonlinear optical phenomena have never been observed by using synchrotron orbital radiation and high harmonics are promising for such investigations. However, the pulse energy of attosecond pulses available so far does not appear to be intense enough to cause nonlinear optical phenomena. In this work, intense attosecond pulses were nonadiabatically generated by using 8-fs blue laser pulses. We have observed the above-threshold ionization (ATI) of rare gases by XUV pulses [2] and demonstrate the autocorrelation measurement of isolated attosecond pulses.

8-fs blue laser pulses producing high harmonics were generated by broadband frequency doubling of Ti:sapphire laser pulses (photon energy 1.55 eV) [3]. Broadband frequency doubling enables us to shorten the pulse duration with high efficiency. The blue laser induces relatively larger nonlinear dipole moment. At the same time, high harmonic pulses rises rapidly nonadiabatically and the field ionization shuts off the harmonic generation, producing intense isolated attosecond pulses.

The ninth harmonic pulses of the blue laser (photon energy 27.9 eV) were generated by focusing the blue laser pulses into Ar gas and were characterized by the autocorrelation technique, in which the two-photon ATI process in helium atoms was used. The ATI process was confirmed by observ-

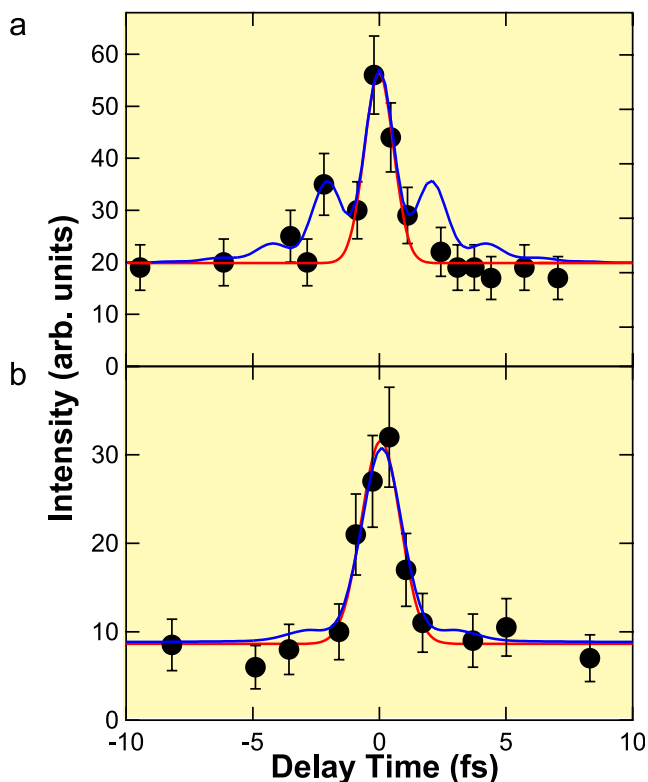


Fig. 1. Autocorrelation traces of the ninth harmonic pulses (27.9 eV): The pulse durations of the driving laser were 8.3 fs (a) and 12 fs (b). The fitting results to the Gaussian function are shown in the red lines. The blue lines are the calculated autocorrelation functions from the spectra.

ing the photoelectrons ejected from helium atoms. The photoelectron yields were recorded as a function of the relative delay time of two high harmonic pulses to form an autocorrelation trace. The results are shown in Fig. 1. The shortest pulse duration obtained was 950 as with pulse energy of 2 nJ [4].

The autocorrelation measurement is the simplest type of pump-probe experiment and is easily extendable to time-resolved spectroscopy. Attosecond time-resolved spectroscopy in the XUV region is expected in the near future.

References

- [1] E. Goulielmakis, M. Uiberacker, R. Kienberger, A. Baltuska, V. Yakovlev, A. Scrinzi, T. Westerwalbesloh, U. Kleineberg, U. Heinzmann, M. Drescher, and F. Krausz, *Science* **305**, 1267 (2004).
- [2] N. Miyamoto, M. Kamei, D. Yoshitomi, T. Kanai, T. Sekikawa, T. Nakajima, and S. Watanabe, *Phys. Rev. Lett.* **93**, 083903 (2004).
- [3] T. Kanai, X. Zhou, T. Sekikawa, S. Watanabe, and T. Togashi, *Opt. Lett.* **28**, 1484 (2003).
- [4] T. Sekikawa, A. Kosuge, T. Kanai, and S. Watanabe, *Nature* **432**, 605 (2004).

Authors

T. Sekikawa, A. Kosuge, T. Kanai, and S. Watanabe

Development of Laser Excited Ultrahigh Resolution Photoemission Spectrometer and the Study of Unconventional Superconductor CeRu₂

Shin Group

It is well known that the variety of properties that conducting materials display stems from the electronic structure at and near Fermi level (E_F). One of the most fascinating

examples is superconductivity, in which the pairing of two electrons makes a tiny energy gap at E_F , leading to unexpected physical properties. Photoemission spectroscopy is a powerful tool to measure the electronic structures. However, being sensitive to surface, such studies have not been able to provide reliable data for f -electron superconductors which exhibit a surface electronic structure different from the bulk[1]. Nonetheless, they exhibit intrinsic but anomalous normal- and superconducting-state properties. Moreover, the extremely small energy scale of the f -electron superconductors has made it difficult to be studied in detail. Escape depth of photoelectron shows strong photon energy dependence and the increase of escape depth using soft x rays has been demonstrated with a resolution of ~ 100 meV. But the value is 100 times larger than the energy scale of superconducting gap. However, as shown in known dependence (universal curve[2]), bulk sensitivity can be achieved to use much lower photon energy (<10 eV). And to get higher energy resolution than He discharge lamp (line width of ~ 1.0 meV) is required to observe the superconducting gap of f -electron systems. To overcome these limitations, we have constructed a new photoemission spectrometer using vacuum-ultraviolet laser as a photon source, as illustrated in Fig. 1(a). The spectrometer system is built using a newly-developed hemispherical electron analyzer (GAMMADATA-SCIENTIA R4000) and laser system producing a high-flux (2.2×10^{15} photons/sec) quasi-continuous-wave (quasi-CW, a repetition rate of 80 MHz) with the highest energy of 6.994 eV developed by Watanabe group (ISSP)[3]. The use of the quasi-CW laser is essential for preventing space-charging effects that broaden energies of photoelectrons. As shown in Fig. 1 (b), an ultrahigh-resolution measurement of a gold Fermi-edge spectrum measured at 2.9 K shows a good correspondence to the convolved Fermi-Dirac function, indicating the energy resolution of $360 \mu\text{eV}$.

Using the newly developed system, we have measured an

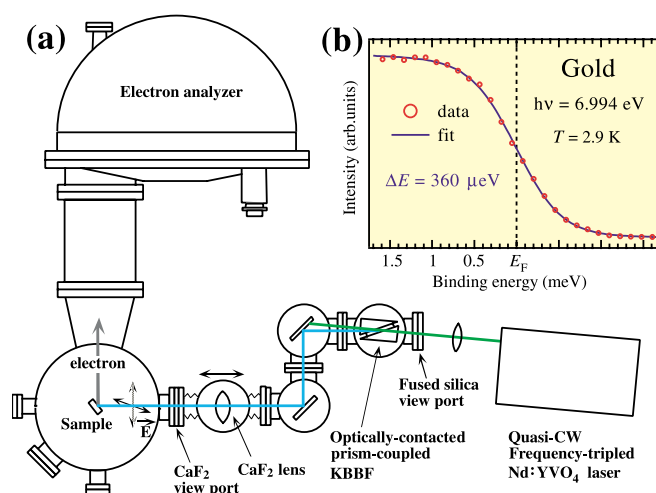


Fig. 1. (a) Schematic diagram of the PES spectrometer system using a laser as a photon source (Laser-PES) and a demonstration of the sub-meV energy resolution. The 2nd harmonic of a quasi-CW frequency-tripled Nd:YVO₃ laser by using an optically-contacted prism-coupled KBe₂BO₃F₂ (KBBF) crystal is focused on a sample with a CaF₂ lens [3]. The kinetic energies of electrons emitted from the sample are measured with a high-precision hemispherical electron analyzer (GAMMADATA-SCIENTIA R-4000). The PES spectrometer and the laser systems are vacuum-separated by a CaF₂ view port, through which the produced 6.994 eV light can be transmitted. (b) Ultrahigh-resolution PES spectrum of an evaporated gold film measured at 2.9 K (red circles), together with the FD function at 2.9 K convolved by a Gaussian with full width at half maximum of $360 \mu\text{eV}$ (a blue line). Total energy resolution of $360 \mu\text{eV}$ was confirmed from the very good match between the experimental and calculated spectra.

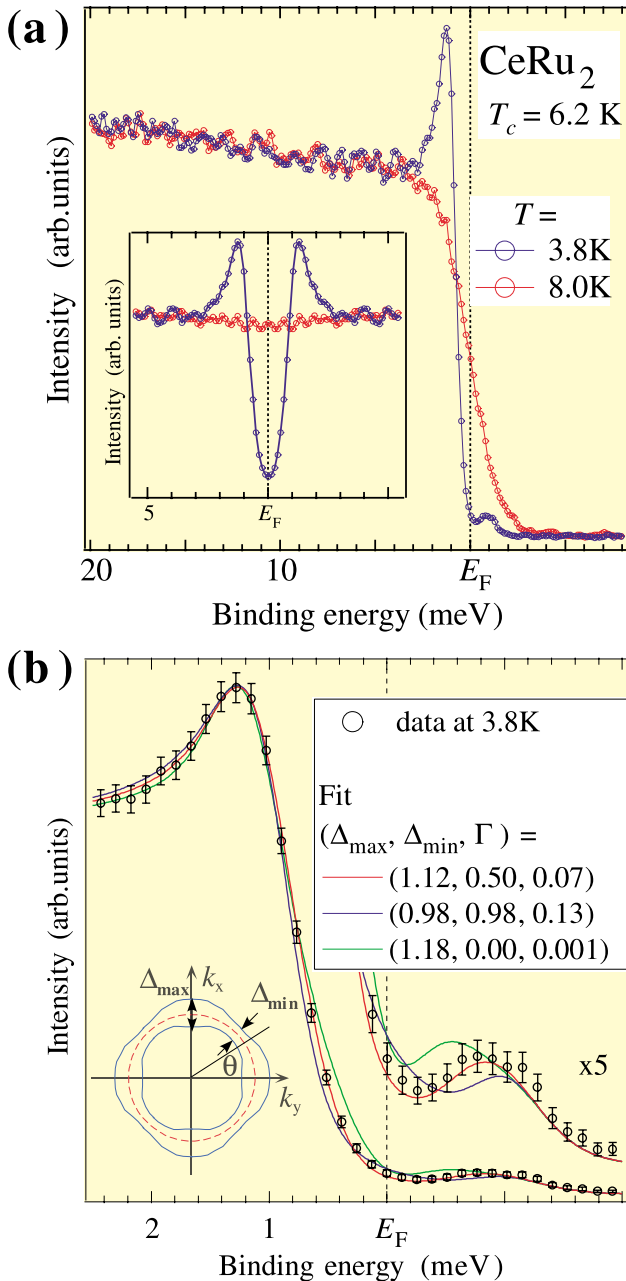


Fig. 2. Ultrahigh-resolution PES data of CeRu₂. (a) T-dependent ultra-high-resolution spectra near E_F with an inset showing the symmetrized spectra from the same data. (b) Normalized SC DOS at 3.9 K compared with calculated spectra. Error bars correspond to square root of intensity. Blue, red, and green lines are results of fittings with anisotropic gaps of a form $\Delta(\theta) = \Delta_{\min} + (\Delta_{\max} - \Delta_{\min}) \times \cos(2\theta)$ of $(\Delta_{\max}, \Delta_{\min}, \Gamma) = (0.98, 0.98, 0.13)$, $(1.12, 0.50, 0.07)$, and $(1.18, 0.00, 0.001)$ in units of meV, where Γ is a thermal broadening parameter and θ the polar angle ($0 \leq \theta \leq \pi/4$). The inset schematically illustrates the anisotropic gap, where a red broken circle represents FS and the distance between blue lines correspond to a gap value.

f-electron superconductor CeRu₂[4], which has the highest T_c (6.2 K) among the Ce compound. High-quality single crystals of CeRu₂ with the residual resistivity ratio of ~ 270 were provided by Prof. Y. Onuki (Osaka Univ.). The total energy resolution for the measurement was set to 520 μeV . Clean surfaces were obtained by fracturing samples in situ ($< 2 \times 10^{-11}$ Torr) at 3.8 K.

In Fig. 2(a), temperature dependent ultrahigh resolution PES spectra across T_c measured with a total energy resolution of 520 μeV are shown. While the spectrum at 8.0 K, normal phase, has a clear Fermi edge, the spectrum at 3.8 K in the superconducting phase shows a sharp peak at

1.35 meV with a leading-edge shift to higher binding energy, indicative of the opening of superconducting gap. The formation of the gap across T_c is more clearly seen in the inset showing symmetrized spectra, which removes the effects of the Fermi-Dirac function. These results constitute the first PES measurement of superconducting electronic structures of an *f*-electron superconductor. Figure 2(b) shows the normalized superconducting spectrum, compared with three calculated spectra with $(\Delta_{\max}, \Delta_{\min}, \Gamma) = (0.98, 0.98, 0.13)$; isotropic case), $(1.12, 0.50, 0.90)$; anisotropic case), $[1.18, 0.00, 0.001]$; maximum anisotropy (nodal) case] in units of meV. Calculated spectrum using an anisotropic gap reproduces the experimental spectrum very well. These analyses indicate the superconducting gap of CeRu₂ has an anisotropy with $\Delta_{\min}/\Delta_{\max}$ ratio of 0.446.

The present success in probing the bulk superconducting electronic structure of an *f*-electron superconductor, CeRu₂ having a delicate surface, using laser PES opens up important opportunities in solid-state physics. First, the technique can be applied to any other material displaying differing surface and bulk electronic states. Second, the laser has a great advantage in the small natural line width (260 μeV) without sacrificing total photon numbers, indicating a great potential for further increase of the energy resolution. This feature is in contrast to other light sources where increasing resolution inherently reduces the intensity. Third, utilizing *k*-resolving capability of PES, one can measure *k*-dependent electronic structures, especially for the *k*-dependent superconducting gap. These characteristics indicate that Laser-PES is a unique experimental probe to study the anisotropic superconducting order parameter of correlated materials. Such studies will reveal the origin of unconventional superconductivity originating in the interplay of localized and itinerant electrons, which is one of the fundamental questions in the condensed matter physics.

References

- [1] A. Sekiyama *et al.*, Solid State Commun. **121**, 561 (2002).
- [2] M. P. Seah and W. A. Dench, Surf. Interface Anal. **1**, 2 (1979).
- [3] T. Togashi *et al.*, Opt. Lett. **28**, 254 (2003).
- [4] T. Kiss *et al.*, Phys. Rev. Lett. **94**, 057001 (2005).

Authors

S. Shin, K. Ishizaka, T. Kiss, T. Yokoya, C. Chen, T. Togashi, and S. Watanabe

Si(111)-6×1-Ag Structure Studied by Surface X-Ray Diffraction

T. Takahashi Group

Metal induced reconstruction of silicon surface attracts much attention from viewpoints of physical interests and applications. In the case of silver on Si(111), it is well known the $\sqrt{3} \times \sqrt{3}$ -Ag surface is formed when one monolayer of silver is deposited on the surface at temperature about 550°C. The 3×1-Ag surface appears after further heating the $\sqrt{3} \times \sqrt{3}$ -Ag surface at about 600°C. The 3×1-Ag structure reversely changes to the 6×1-Ag structure at room temperature. Whereas the $\sqrt{3} \times \sqrt{3}$ -Ag structure is well established after a long controversy [1], the structure of the 3×1 and 6×1 [2] remains ambiguities.

Metal induced 3×1 structures appear on Si(111) for alkali metals such as Li, Na, K and Mg. The honeycomb-chain channel model [3] is most probable for those 3×1 structures

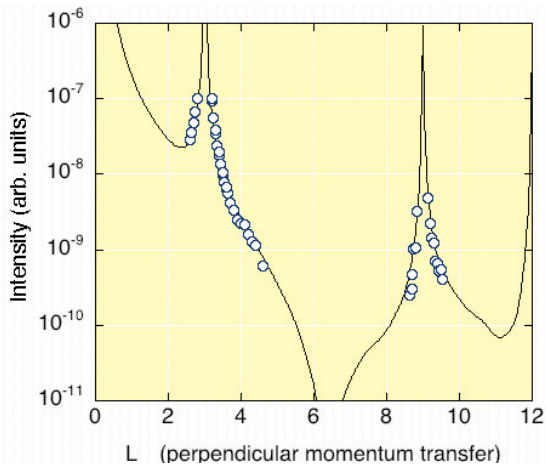


Fig. 1. Intensity along 00 rod from the Si(111)-6×1-Ag surface. Circles indicate measured intensities, and solid curve is the calculated one for the best fit model shown in Fig. 2.

where metals are arranged in a chain, but the atomic arrangement of the 3×1 structure for Ag is not studied compared to those alkali metal induced surfaces.

In this work we study the perpendicular structure of the 6×1-Ag surface by the measurement of X-ray crystal truncation rod scattering. Experiments were made using the six-circle diffractometer install in the beam line 15B2 of the Photon Factory. It is essential to measure the diffraction intensity at points with large perpendicular momentum transfer to determine the structure with high resolution. Figure 1 shows the diffraction intensities measured along the 00 rod. Sharp peaks at $L=3$ and 9 correspond 111 to and 333 Bragg reflections, respectively. The intensity change shows a strong asymmetry around 333 Bragg reflection. Intensities at some range between Bragg points were less than the background level. This weak intensity comes from the destructive interference between surface layers and the substrate, and thus suggests that the perpendicular structure is rather simple.

The analysis was done based on the 3×1 structure because the perpendicular structures are expected to change little in the phase transition between 3×1 and 6×1 structures. In the analysis we tried some models with different Si density. Least squares fits were done for each model by changing the height of Ag and Si atoms where the coverage of Ag was fixed to 1/3. The best fit was obtained for the model where four Si atoms in the 3×1 structure are located almost in the same height as illustrated in Fig. 2. The height of reconstructed Ag and Si atoms from the substrate was 3.0 Å and 2.3 Å, respectively. These values are almost the same those obtained for the $\sqrt{3} \times \sqrt{3}$ -Ag structure. This means that the perpendicular structure changes little as the structural changes from $\sqrt{3} \times \sqrt{3}$ to 3×1.

References

- [1] T. Takahashi and S. Nakatani, Surf. Sci. **282**, 17 (1993).
- [2] C. Collazo-Davila *et al.*, Phys. Rev. Lett. **80**, 1678 (1998).
- [3] S. C. Erwin, Phys. Rev. Lett. **75**, 1973 (1995).

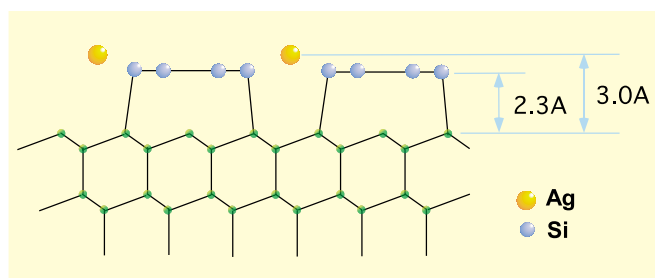


Fig. 2. Side view of the best fit model for the Si(111)-6×1-Ag surface.

Authors

K. Sumitani, T. Hoshino, K. Masuzawa, Y. Nodumi, S. Nakatani, H. Tajiri^a, K. Akimoto^b, H. Sugiyama^c, X. Zhang^c, and H. Kawata^c
^a JASRI/Spring-8
^b Nagoya University
^c KEK-PF

Strong Optical Absorption by a Single Quantum Wire

Akiyama Group

A direct measurement of optical absorption by a nanometer-scale quantum wire has been one of the major challenges in nano-science. We have recently performed such an experiment, and observed strong optical absorption by a single quantum wire: About 98% of incident light is absorbed by a $14\text{nm} \times 6\text{nm}$ single GaAs quantum wire of $500\mu\text{m}$ -length, though the wire is much smaller than a floating dust in air!

A quantum wire (T-wire) is formed at a T-shaped intersection of two GaAs/AlGaAs quantum wells, as shown in inset of Fig. 1(a). The red contour curves show the wavefunction of electrons confined in a $14\text{nm} \times 6\text{nm}$ lateralized wire. The T-wire is embedded coaxially in the center of an optical waveguide. Length of the T-wire and the waveguide is $500\mu\text{m}$. In the absorption measurement, incident light goes into the waveguide from one end, travels $500\mu\text{m}$ along the T-wire, and comes out from the other end of the waveguide. Coupling efficiency of the incident light is 24%, and the T-wire optical-confinement factor $\Gamma = 4.6 \times 10^{-4}$.

Figure 1(a) shows the transmittance spectrum for the single T-wire around the band gap at 5 K, where strong

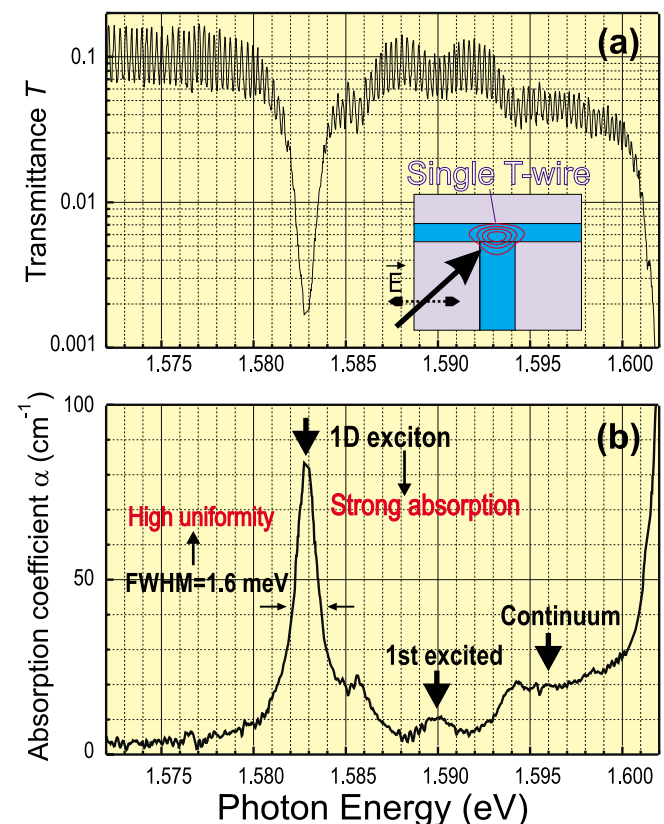


Fig. 1. (a) The transmittance spectrum for a single T-wire at 5 K. The inset shows the T-wire structure and transmission light with horizontal polarization. (b) The absorption spectrum derived from the transmittance spectrum. The 1D exciton shows a strong and narrow absorption peak.

attenuation is observed at 1.5828 eV and above 1.600 eV. In the other region, we observe clear Fabry-Perot oscillations. Figure 1(b) shows the absorption spectrum for the single T-wire derived from the transmittance spectrum. Three absorption structures of the 1D exciton, the excited state of 1D exciton, and the 1D continuum states, are resolved. The absorption peak of 1D exciton has a width of 1.6 meV. The absolute value of absorption for 1D exciton shows $\alpha=80 \text{ cm}^{-1}$. This value gives $e^{-\alpha L} = 0.018$ for waveguide length $L=500 \mu\text{m}$, which means that 98% transmission light is absorbed by a single pass of the 500- μm -long waveguide in spite of the small confinement factor Γ . This demonstrates strong excitonic absorption of the single T-wire.

Reference

[1] Y. Takahashi, *et al.*, Appl. Phys. Lett. **86**, 243101 (2005); CLEO/QELS2005, Baltimore, USA, May 2005.

Authors

Y. Takahashi, Y. Hayamizu, H. Itoh, M. Yoshita, H. Akiyama, L. Pfeiffer^a, and K. West^a
^a Bell laboratories, Lucent Technologies, USA

Optical Study of a Single-Quantum-Wire FET

Akiyama Group

Optical investigations of a single-quantum-wire field-effect transistor (FET), that is an n-type modulation-doped single T-shaped quantum wire with tunable 1D electron density via gate voltages, are made via photoluminescence (PL) and PL excitation (PLE) spectroscopy at 5 K. The sample structure and experimental setup are schematically shown in Fig. 1.

The measured PL and PLE spectra at various gate voltages (V_g) are shown in Fig.2 (a). The evolution of these

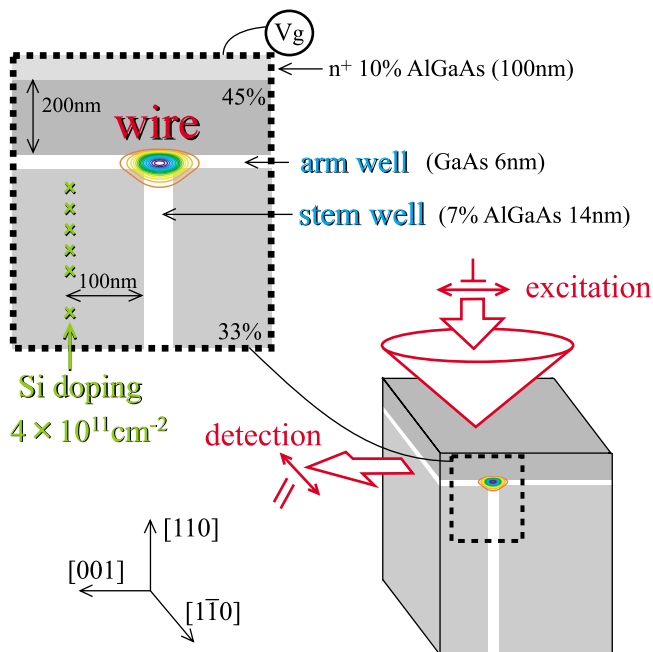


Fig. 1. Schematic structure of n-type doped T-shaped quantum wire. The cross-sectional region of 14nm quantum well (stem well) and 6nm quantum well (arm well) works as a 1D wire. The stem well is modulation doped and connected to the ground level. We tune 1D electron density in the wire by applying gate voltage (V_g). Excitation and detection are perpendicular to each other both in light directions and in polarizations, to eliminate intense laser-scattering noises.

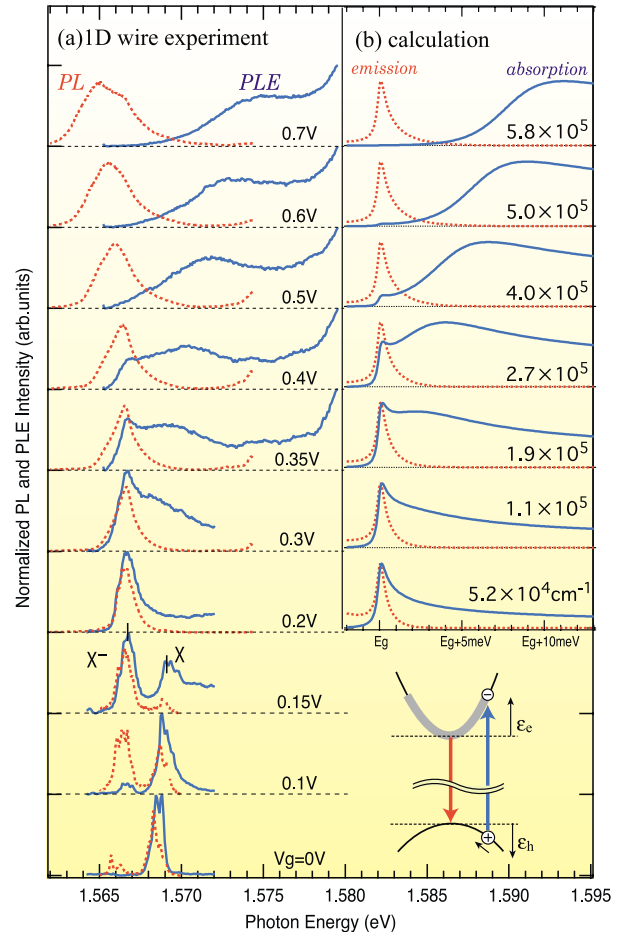


Fig. 2. Experimental (a) and theoretical (b) spectra of PL (red) and PLE (blue), where 1D electron density increases with the applied gate voltage. Each spectrum is normalized by peak intensity. The evolution of the spectra shows metal-insulator crossover, where the peaks of excitons (X) and trions (X^-) evolve to band-to-band transitions in the presence of an electron plasma. The theoretical curves are calculated with the free-particle approximation.

spectra shows the metal-insulator crossover from excitonic discrete peaks to band-to-band transitions with large Burstein-Moss shifts. The PL and PLE spectra in the band-to-band transition regime are compared with a calculation based on the free-particle approximation, as shown in Fig. 2 (b).

In low-density regime ($V_g=0-0.2\text{V}$), we observed complete oscillator-strength transfer from excitons (X) to trions (X^-). At high-density regime ($V_g=0.5-0.7\text{V}$), a broad absorption onset corresponding to the Fermi edge shows blue shift with increased density. In the crossover region from trion to band-to-band transition ($V_g=0.3-0.4\text{V}$), we found a double peak structure corresponding to the Fermi edge and square root divergence of 1D density of states. These spectral features demonstrate bound-state formation and carrier population in inverse-square-root density of states inherent to 1D systems.

Reference

[1] T. Ihara *et al.*, The 27th international conference on the physics of semiconductors (ICPS-27), Flagstaff, USA, July 2004.

Authors

T. Ihara, Y. Hayamizu, M. Yoshita, H. Akiyama, L. N. Pfeiffer^a, and K. W. West^a
^a Bell laboratories, Lucent Technologies, USA

Magnetic Dead Layers Induced by Strain at Fct Fe/Rh(001) Interface

Kakizaki group

It is known that in Fe films grown epitaxially on a substrate with a large lattice misfit, a strain at the interface causes the elastic deformation of the films, *i.e.* the Poisson effect, and leads to face-centered-tetragonal (fct) structure. The strain at the interface is released during the film growth by the change of the lattice constant or by the dislocation at the interface, which modifies the structural and magnetic phases of the Fe films. It has been theoretically shown that fcc and fct Fe manifest diverse magnetic phases depending on the lattice constants [1-3]. Recently we studied the structure and magnetism of the Fe films grown on the Rh(001) substrate ($a_0=3.80 \text{ \AA}$) with a relatively large lattice misfit [4, 5]. The structure of the Fe film reveals fct(001) compressed along the direction perpendicular to the surface in low coverage region and gradually changes to distorted bcc(110) as the film thickness increases. To investigate the relationship between the structure and magnetism during the film growth,

State	$E-E_{\text{fcc FM Fe}}$ (mRy / atom)	Lattice Constant (\AA)	c/a
fcc AF	0.456	3.49	
fcc FM	0.000	3.63	
fct NM	27.770	$a=b=3.84, c=3.18$	
fct AF	14.558	$a=b=3.84, c=3.33$	
fct FM	6.049	$a=b=3.84, c=3.18$	0.83

Table 1. Total energy minimum, E , for the NM, AF, and FM phases of fcc, and fct Fe. The values are presented after subtracting the minimum energy for fcc FM Fe, $E_{\text{fcc FM Fe}}$. Lattice constants (a , b , and c) and ratio of c/a at the minimum energies are also shown.

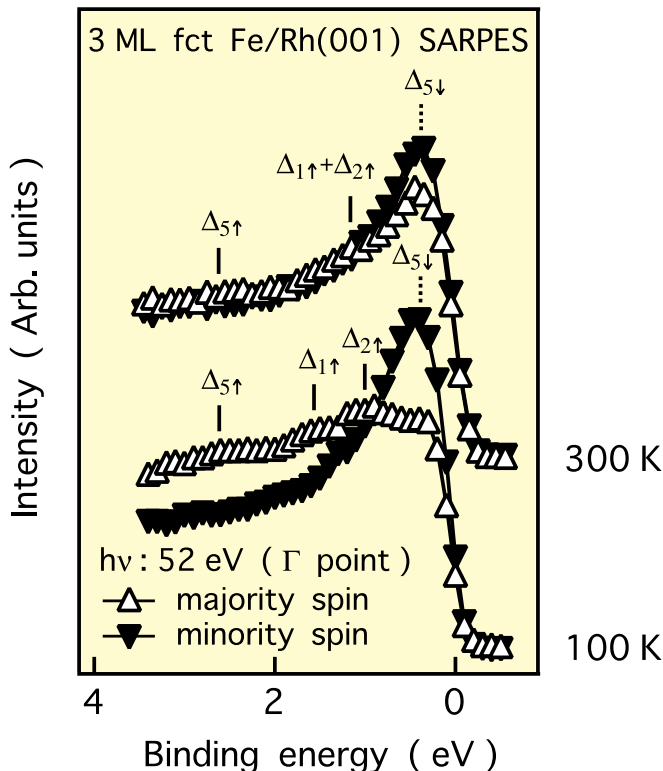


Fig. 1. SARPES of 3ML Fe/Rh(001) at 100K and at RT. The binding energies of the spectral features in the majority and minority spin spectra are indicated by vertical bars with corresponding valence bands.

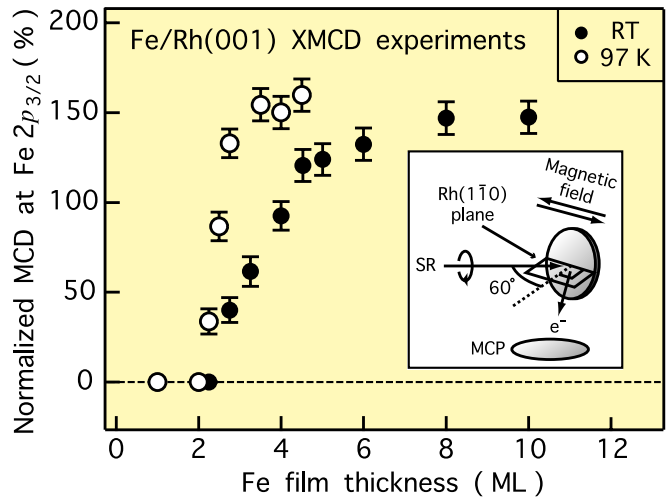


Fig. 2. Thickness dependence of XMCD signals of the Fe/Rh(001) system measured at Fe $2p_{3/2}$ absorption edges. The inserted figure illustrates the geometry of the XMCD experiments.

we have made band structure calculations, spin- and angle-resolved photoelectron spectroscopy (SARPES) and soft X-ray magnetic circular dichroism (XMCD) experiments.

We have calculated the total energies of three different magnetic phases, *i.e.* nonmagnetic (NM), antiferromagnetic (AF) and ferromagnetic (FM) phases, as a function of an out-of-plane lattice constant c . The results show that the total energy minimum for FM phase is smaller than those for AF and NM phases. Since the ratio of c/a at this equilibrium state is very close to those of 4 ML and 5 ML Fe films ($c/a=0.84$), which were evaluated by the X-ray photoelectron diffraction experiments [4], we conclude that 4 ML and 5 ML Fe films on the Rh(001) surface are in a fct structure and FM. We have measured the SARPES spectra of the Fe films with various film thicknesses. It was observed that in Fe films over 3 ML, the distinct majority and minority spin spectra are observed even at RT, which reveals that Fe films are magnetically live layers, *i.e.* FM. The T_C of the film, which is estimated by temperature dependence of the spin polarization of the spectral features, increases with film thickness and reaches to the value of bulk bcc Fe (1043 K) at about 6 ML. We also found that T_C falls to 0 K in 2 ML film thickness, which implies that the Fe films below 2 ML are magnetic dead layers. To confirm above observation we have measured the thickness dependence of the XMCD signals at Fe $2p_{3/2}$ absorption edges, and found that the XMCD signals observed for Fe films below 2 ML are smaller than the detection limit. The results are consistent with those observed in the thickness dependence of T_C and confirms the existence of the magnetic dead layers in the Fe films induced by strain at the interface.

References

- [1] V. L. Moruzzi, P. M. Marcus, and J. Kübler, Phys. Rev. B **39**, 6957 (1989).
- [2] T. Asada and K. Terakura, Phys. Rev. B **46**, 13599 (1992).
- [3] S. L. Qiu and P. M. Marcus, Phys. Rev. B **60**, 14533 (1999).
- [4] K. Hayashi, M. Sawada, A. Harasawa, A. Kimura, and A. Kakizaki, Phys. Rev. B **64**, 054417 (2001).
- [5] K. Hayashi, M. Sawada, H. Yamagami, and A. Kakizaki, J. Phys. Soc. Jpn. **73**, 2550 (2004).

Authors

K. Hayashi, M. Sawada, H. Yamagami, and A. Kakizaki

New Orbit Correction Method for Beam Stabilization in High-Brilliance Synchrotron Light Sources

Nakamura Group

A new orbit correction method that we proposed and formulated, the eigenvector method with constraints (EVC) [1], is very suitable for orbit feedback scheme of beam stabilization in high-brilliance synchrotron light sources and has many advantages. The EVC can more tightly fix beam positions at light source points such as insertion devices than the ordinary eigenvector method (EV) and also reduce the closed orbit distortion (COD) of the whole ring like the EV. Namely the EVC has both functions of exact local orbit correction for light source points and global orbit correction for the whole ring.

Computer simulations successfully demonstrate the features of the EVC. Figure 1 shows simulated vertical CODs of the Super-SOR ring before and after correction by the EVC and EV. Both methods much reduce the global COD of the ring. The constraint conditions of the EVC in this simulation are that the beam positions at 28 beam position monitors(BPMs) on both sides of 14 long straight sections used for insertion devices are zero. Figure 1a shows that the EVC corrects all the beam positions and angles of the 14 light source points to zero, while the EV cannot completely correct the COD at the 28 BPMs, as shown in Fig. 1b. The EVC can also be applied to the stabilization of the photon beam positions at the SR beamlines. The EVC requires only one

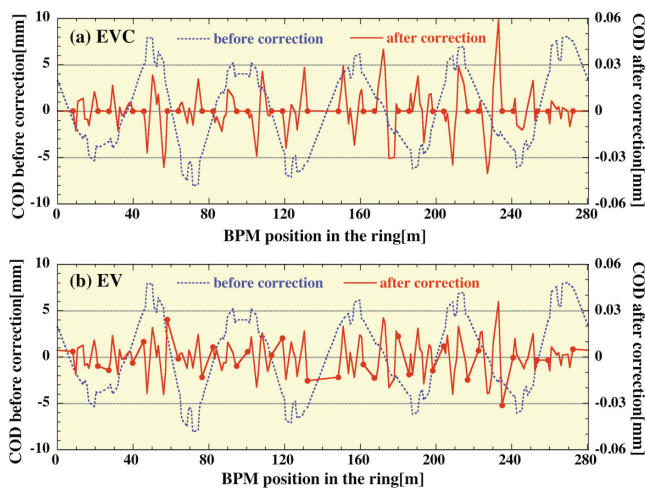


Fig. 1. Vertical closed orbits of the Super-SOR ring before and after correction by (a) the EVC and (b) the EV. The solid circles indicate 28 beam positions at the constrained BPMs after correction.

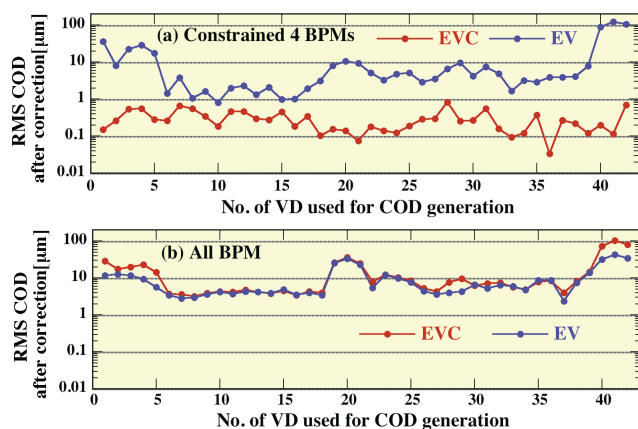


Fig. 2. The RMS COD values for (a) the constrained four BPMs and (b) all the BPMs after correction by the EVC and the EV at the PF ring.

feedback loop or system for the beam stabilization at many light source points. Thus the cost and manpower for the beam stabilization can be much reduced by adopting the EVC.

The EVC was experimentally studied in the PF ring and the PF-AR ring at KEK in order to demonstrate the effectiveness of the EVC in "real machines" with various errors and nonlinearities. The PF ring has 65 BPMs for COD measurement, 42 vertical dipoles(VDs) for usual vertical orbit correction and 28 fast vertical steering magnets(FVSs) for global orbit feedback. The vertical COD generated by each of 42 VDs was corrected by 28 FVSs in this study. The constraint conditions of the EVC are that the beam positions at 4 BPMs on both sides of two insertion devices are zero. The study results of the PF ring are shown in Fig. 2. Figure 2a clearly shows that the EVC corrects all of the RMS(root mean square) CODs for the constrained 4 BPMs to a sub-micron level, while the EV cannot reduce all of the RMS CODs to this level. On the other hand, there is no clear difference between the EVC and EV in the RMS CODs for all the BPMs, as shown in Fig. 2b. Similar results were also obtained in the machine study of the PF-AR ring. The EVC worked well in these real machines in spite of the various existing errors and nonlinearities. These results demonstrate that the EVC is very effective and useful for orbit correction and beam stabilization in synchrotron light sources.

Reference

[1] M. Satoh, Y. Kamiya, and N. Nakamura, Proc. of EPAC98, Stockholm, 1998, pp.1723-1725.; Y. Kamiya, N. Nakamura, and M. Satoh, Proc. of PAC99, New York, 1999, pp.1174-1176.

Authors

N. Nakamura, H. Takaki, H. Sakai, K. Harada^a, and T. Obina^a
^a High Energy Accelerator Research Organization(KEK)

Small-angle Neutron Scattering Study on Pressure-Sensitive Polymer Gels

Shibayama Group

Poly(*N*-isopropyl acrylamide) (PNIPA) hydrogel is one of the most well-known thermosensitive gels that undergo a volume phase transition at 34°C [1, 2] The temperature sensitivity of the PNIPA gel is ascribed to the hydrophobicity of the *N*-isopropyl groups located on the side chain. At low temperatures, PNIPA chains are solvated in water owing to "iceberg structure" formation of water surrounding the

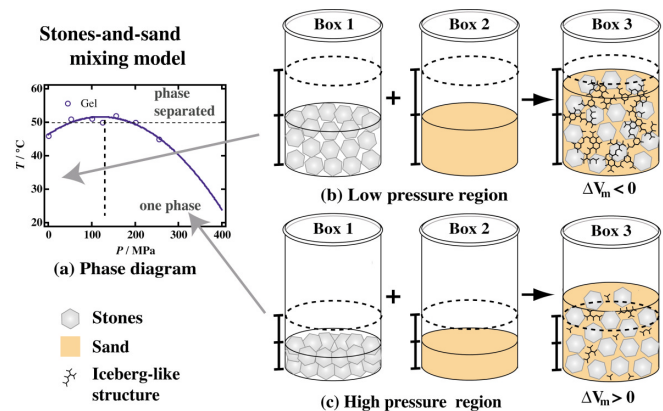


Fig. 1. (a) P - T phase diagram of a 7 wt % PNIPA-AAc weakly charged hydrogels. (b) and (c) are the stone-and-sand model explaining the origin of convexity of the phase behavior.

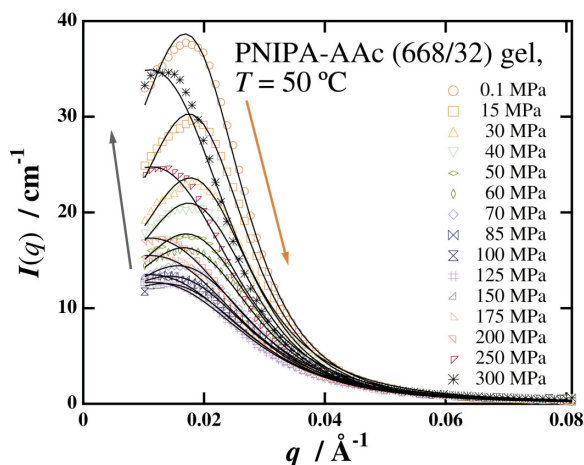


Fig. 2. SANS intensity functions of PNIPA-AAc hydrogels at 50°C obtained at various pressures. Note that $I(q)$ has a peak at $q \simeq 0.02 \text{ \AA}^{-1}$ and the peak shifts toward higher q and decreases with increasing P up to P_c and increases with further increasing P . The solid lines denote the calculated scattering functions with Panyukov-Rabin theory.

hydrophobic N-isopropyl groups. An increase of temperature leads to melting of the iceberg structure, resulting in aggregation of PNIPAA chains followed by gel collapsing. Introduction of charges to PNIPAA chains leads to an increase in the transition temperature as well as an increase of the gap between the swollen and collapsed phases more than a factor of 100 folds by volume. Because of these unique properties, various applications have been proposed, such as intelligent drug delivery systems, sensors of various diseases, recollecting agents of rare and/or toxic metals, etc. Since iceberg formation accompanies a positive volume change, the transition is expected to be pressure sensitive. We carried out small-angle neutron scattering (SANS) experiments in order to investigate the microscopic structure of hydrogels undergoing volume phase transition by temperature and/or pressure. SANS studies were carried out on weakly charged poly(*N*-isopropyl acrylamide-co-acrylic acid) (PNIPAAc) gels. The phase diagram was determined in the pressure-temperature (P - T) plane by light scattering.

Fig.1(a) shows the P - T phase diagram of a 7 wt% PNIPAAc gel. The phase diagram is a parabolic function, having maximum at ($P_c = 100.2 \text{ MPa}$, $T_c = 54.7 \text{ °C}$). It is quite interesting that the P - T curve has a maximum. Fig.1(b) and (c) show the stone-and-sand model that accounts for the convexity. At atmospheric pressure, a negative volume change of mixing, $\Delta V_m < 0$, was obtained. Hence, the following inequality is deduced, $\Delta V_m \gg \Delta V_{m,ice}$, where $\Delta V_{m,ice}$ is the volume change associated with iceberg formation. Since, the iceberg formation is exothermic and the enthalpy of mixing, ΔH_m , is negative, $dT/dP = TdV_m/dH_m$ is positive. This is why the phase diagram has a positive slope. However, ΔV_m is expected to be positive at high pressures, resulting in a change of the slope to negative above P_c [3].

SANS experiments were carried out according to the P - T phase diagram. At low temperature and pressure region, where the systems were in one phase, the scattering intensity functions, $I(q)$ s, were well described with Ornstein-Zernike functions. However, when SANS intensity functions were collected at 50°C along the horizontal dashed line shown in Fig.1(a), an re-entrant behavior was observed. As shown in Fig.2 a scattering maximum appeared in $I(q)$ s at $P = 0.1 \text{ MPa}$. This scattering maximum is due to microphase separation as a result of antagonism between the electrostatic and hydrophobic interactions. However, as P increased, the

peak disappeared at $P \simeq 100 \text{ MPa}$, and then reappeared by further increase in P . The scattering functions were successfully reproduced with the Panyukov-Rabin theory for polymer gels with frozen-inhomogeneities[5].

The analysis indicated that the convexity is due to the quadratic nature of the polymer-solvent interaction with respect to P as a result of strong pressure dependence of iceberg formation.

References

- [1] Y. Hirokawa and T. Tanaka, *J. Chem. Phys.* **81**, 6379 (1984).
- [2] M. Shibayama, T. Tanaka, and C. C. Han, *Macromolecules* **97**, 6829 (1992).
- [3] I. Nasimova, T. Karino, S. Okabe, M. Nagao, and M. Shibayama, *Macromolecules* **37**, 8721 (2004).
- [4] I. Nasimova, T. Karino, S. Okabe, M. Nagao, and M. Shibayama, *J. Chem. Phys.* **121**, 9708 (2004).
- [5] S. Panyukov and Y. Rabin, *Phys. Rep.* **269**, 1 (1996).

Authors

I. Nasimova^a, T. Karino, S. Okabe, M. Nagao, and M. Shibayama
^a Moscow State University

Glass Transitions of Room-temperature Ionic Liquids

Yamamuro Group

Ionic compounds usually have melting temperatures T_m higher than room temperature because of their strong and long-range interionic interactions. Recently, it was found that a series of organic ionic compounds have T_m lower than room temperature and they are called "room temperature ionic liquids" or simply "ionic liquids". These compounds have various useful properties as a solvent, e.g., low vapor-pressure, high solubility for both hydrophilic and hydrophobic solutes, etc. In spite of a number of research focusing attention on their application, few studies on their basic physical properties have been done. We have measured heat

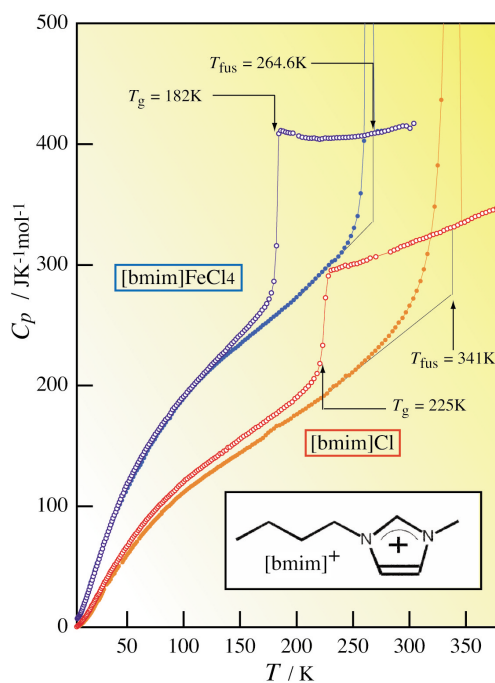


Fig. 1. Molar heat capacities of [bmim]Cl and [bmim]FeCl₄ measured with an adiabatic calorimeter in Yamamuro laboratory. Open symbols denote the data of glassy and liquid states and closed symbols those of crystalline one. T_g and T_{fus} represent glass transition and fusion temperatures, respectively. The inset shows the structure of [bmim]⁺ ion.

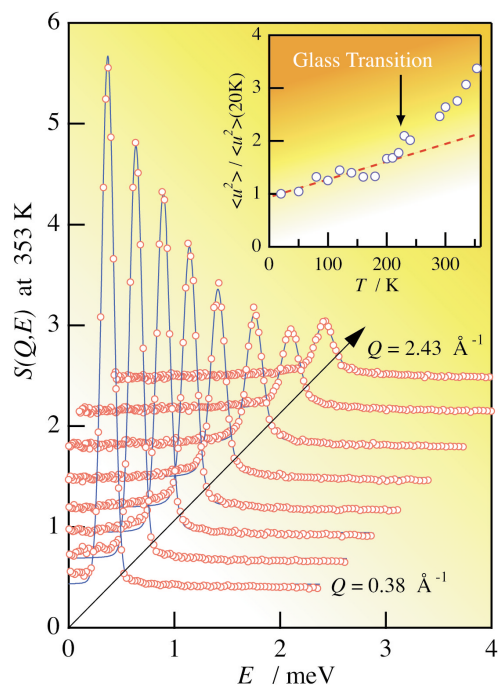


Fig. 2. Quasielastic neutron scattering spectra of [bmim]Cl measured at 353 K for several momentum transfer values on AGNES spectrometer of ISSP. The data are fitted to Lorentzian functions to obtain self-diffusion coefficients. The inset gives the temperature dependence of the mean square displacements divided by the value at 20 K.

capacities and neutron scattering spectra of some salts of 1-butyl-3-methylimidazolium ion [bmim]⁺, which is a typical cation of ionic liquids [1].

Fig. 1 shows the heat capacities C_p of [bmim]Cl and [bmim]FeCl₄. The former compound is important as a prototype ionic liquid and the latter is recently remarked as a magnetic ionic liquid [2]. A glass transition with a large C_p jump was found at 225 K in [bmim]Cl and 182 K in [bmim]FeCl₄. It is of interest that the fusion of [bmim]FeCl₄ is much sharper than that of [bmim]Cl. The temperature dependence of configurational entropy, obtained by integrating C_p/T with T , demonstrated that both ionic liquids are of "fragile liquids" (liquids with highly disordered structures largely changing with temperature) as molecular and polymer liquids. This result was quite unexpected since the ionic interaction generally causes ordering of liquid structure.

In both ionic liquids, quasielastic neutron scattering (Q -dependent broadening of elastic peaks) was observed as shown in Fig. 2. The inset reveals an anomalous increase of $\langle u^2 \rangle$ showing an onset of some fast relaxation process around T_g . Self-diffusion coefficients D_s were derived from the data in Fig. 2. The activation energy calculated from the temperature dependence of D_s is 11 kJ/mol, which is considerably smaller than that of the intramolecular rotation of butyl-group in organic molecules, 13-15 kJ/mol.

Both calorimetric and neutron scattering data clearly revealed that the butyl-group of [bmim]⁺ ion is highly disordered and flexible, and entropically stabilizing ionic liquid phase. This can be an origin of low melting temperatures of ionic liquids which is the most significant question in the science of ionic liquids.

References

- [1] O. Yamamuro, Y. Inamura, S. Hayashi, and H. Hamaguchi, J. Chem. Phys., submitted.
- [2] S. Hayashi and H. Hamaguchi, Chem. Lett. **33**, 1590 (2004).

Authors

O. Yamamuro, Y. Inamura, S. Hayashi^a, and H. Hamaguchi^a
^a Graduate School of Science, University of Tokyo

Slow Dynamics in Superparamagnets, Superspin Glasses, and Spin Glasses

Takayama Group

Relatively dense ferromagnetic nanoparticle systems, now called superspin glasses, exhibit slow dynamics which is qualitatively indistinguishable from that observed in (atomic) spin glasses and its origin is attributed to frustrating and random dipole interactions among particle moments (superspins). However, even in dilute nanoparticle systems where the dipole interactions are vanishingly small (superparamagnets), rather similar slow dynamics is often observed. We have argued that such slow dynamics originates solely from a broad distribution of relaxation times which comes from that of the anisotropy energy barriers against superspins, which in turn are assumed to be proportional to nanoparticle volume V . In fact, the master equation for each superspin magnetization $M(t;V)$ is easily solved including its history of temperature $T[t]$ and field $h[t]$ up to time t , and peculiar slow dynamics, such as the memory effect shown in Fig. 1, can be reproduced by integrating $M(t;V)$ with an appropriate V -distribution [1,2].

A qualitative difference in slow dynamics in superparamagnets and superspin glasses is clearly seen in the zero-field-cooled (ZFC) process, since $M(t;V)$ remains zero in the former when it starts with $M(0;V) = 0$, while the spin-glass (SG) order grows in the latter whose effect can be observed after the process. Another interesting difference is seen in the field-cooled magnetization (FCM) at T lower than the (rounded) cusp temperature: FCM of superparamagnets continues to increase by further decreasing T (Fig. 1), while FCM of most of (super)spin glasses tends to decrease though a little in magnitude. The latter feature, we have argued [3], is interpreted as an indication of non-equilibrium nature of the FC process which has been roughly considered to be equilibrium one as compared with the non-equilibrium ZFC process.

Between slow dynamics in superspin glasses and spin glasses there exists the following difference. We have tried to observe experimentally the rejuvenation effect, i.e., the sensitivity of the SG state on a T -change seen in spin glasses, in a superspin glass without success on proving its presence

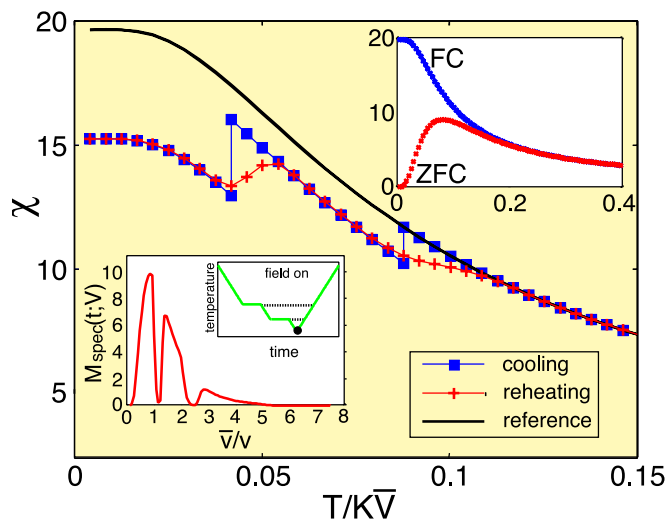


Fig. 1. Memory effect of a superparamagnet which is field-cooled with two intermittent stops when h is set zero. In the spectrum of $M(t;V)$ at the lowest temperature the effect of the stops are clearly imprinted (lower-left inset), and its magnetization nearly follows the cooling curve when the system is reheated. In the upper-right inset the FCM and ZFCM of the system are shown.

[4]. The result is attributed to a quantitative difference in time scales of experiments t_{obs} relative to a microscopic (super)spin flip time t_0 . Namely, since t_0 's of superspins, which are governed by thermal activated processes, are much longer than t_0 's of atomic spins, in order to observe the rejuvenation effect within a common magnitudes of T -change, we have to set t_{obs} much longer than the experimental time that we could use.

The qualitative and quantitative differences above discussed are important to get a proper understanding of slow dynamics in SG-related materials and other complex systems as well.

References

- [1] M. Sasaki *et al.*, Phys. Rev. Lett. **93** 139701 (2004).
- [2] M. Sasaki *et al.*, Phys. Rev. B **71** 104405 (2005).
- [3] P. E. Jönsson and H. Takayama, J. Phys. Soc. Jpn. **74** 1131 (2005).
- [4] P. E. Jönsson *et al.*, Phys. Rev. B **71** 104404 (2005).

Authors

M. Sasaki, P. E. Jönsson, P. Nordblad, H. Mamiya, H. Yoshino, and H. Takayama

Room Temperature CMR beyond 1000% in the A-site Ordered Perovskite Manganite

Y. Ueda Group

We have successfully achieved colossal magnetoresistance (CMR) beyond 1000% at room temperature in perovskite manganese oxides, as shown in Fig. 1. For the last decade, magnetoresistance (MR) effect has been extensively investigated from various view points of not only fundamental solid state physics but also application in electronic devices. Many MR materials have been discovered as in granular films, tunneling junctions and transition metal oxides. Especially, the research of MR oxides has been focused on the perovskite manganites, $R_{1-x}A_x\text{MnO}_3$ (R = rare earth elements and A = Ca, Sr and Ba), because they exhibit CMR associated with the competition between charge/orbital

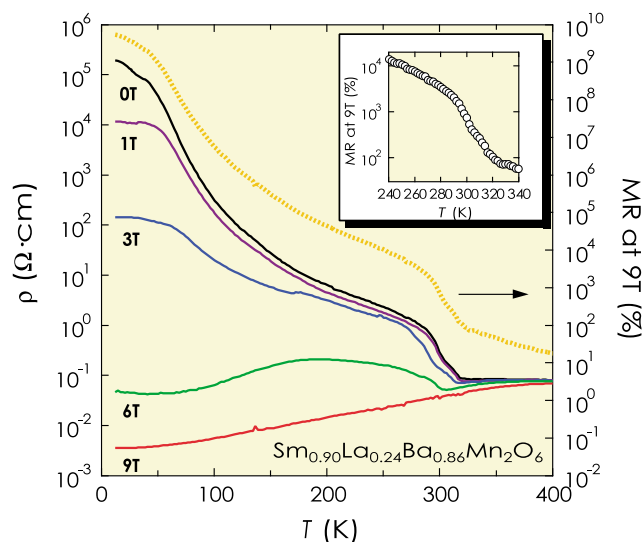


Fig. 1. Temperature dependences of resistivity under various magnetic fields and magnetoresistance MR(%) at 9 T in single crystal of $\text{Sm}_{0.90}\text{La}_{0.24}\text{Ba}_{0.86}\text{Mn}_2\text{O}_6$. The system shows a metal-insulator transition around 320 K under no magnetic field. The resistivity of the insulator phase decreases with increasing magnetic field and the system becomes metallic at 9 T in the whole temperature range. The inset shows MR(%) at 9 T around room temperature. The MR(%) is beyond 1000% at room temperature. This is the record of MR effect in transition metal CMR oxides.

order (CO) and ferromagnetic metal (FM) generated by the double exchange interaction. However, the manganites with CMR such as $\text{La}_{1-x}\text{Ca}_x\text{MnO}_3$ and $(\text{Nd,Sm})_{0.5}\text{Sr}_{0.5}\text{MnO}_3$ have a disadvantage of application; the CMR appears far below room temperature. Therefore, it has been desired to explore new materials with CMR around room temperature.

Recently we successfully synthesized the A-site ordered Ba-based manganites, RBaMn_2O_6 [1-3]. RBaMn_2O_6 has a layer-type order of R^{3+} and Ba^{2+} ions in the structure and as a result the MnO_2 square-lattice is sandwiched by two types of rock-salt layers, RO and BaO, with different sizes. The FM is dominant in RBaMn_2O_6 (R = La, Pr and Nd) with relatively small mismatch between RO and BaO lattices, while in RBaMn_2O_6 (R = Sm ~ Ho, Y) with large mismatch, the CE-type CO insulator (COI) is stabilized at the remarkably high temperatures (T_{CO}) far above 300 K. Such high T_{CO} could mainly originate from the absence of electrostatic potential disorder at the A-sites in the layer-type order of R^{3+} and Ba^{2+} . Since CMR is related to the conversion of COI phase to FM phase under magnetic fields, MR effect above room temperature is expected in RBaMn_2O_6 . $\text{SmBaMn}_2\text{O}_6$ with $T_{\text{CO}} = 375$ K is a candidate because it is located near FM region in the electronic phase diagram of RBaMn_2O_6 . However the COI phase itself in $\text{SmBaMn}_2\text{O}_6$ is very tough and MR effect is not observed even at 9 T. We have engaged in the realization of CMR at room temperature by introducing some sophisticated disorder to $\text{SmBaMn}_2\text{O}_6$. We have achieved the record of MR effect over 340% in the sintered $\text{Sm}_{0.90}\text{La}_{0.24}\text{Ba}_{0.86}\text{Mn}_2\text{O}_6$ and beyond 1000% in its single crystal under 9 T at room temperature, where MR(%) is given by $\text{MR}(\%) = \{[\rho(0) - \rho(H)] / \rho(H)\} \times 100\%$; $\rho(H)$ and $\rho(0)$ are the resistivity under 9 T and zero magnetic field, respectively. The MR effect about 340 % is, to the best of our knowledge, the highest among MR(%) reported in transition metal CMR oxides. In the single crystal, the COI is perfectly converted to FM, showing the remarkable CMR beyond 1000% at room temperature. The MR efficiency under much lower magnetic fields can be expected in thin films of the system.

References

- [1] T. Nakajima, H. Kageyama, H. Yoshizawa, and Y. Ueda, J. Phys. Soc. Jpn. **71**, 2843 (2002).
- [2] T. Nakajima, H. Kageyama, H. Yoshizawa, K. Ohya, and Y. Ueda, J. Phys. Soc. Jpn. **72**, 3237 (2003).
- [3] T. Nakajima, H. Yoshizawa, and Y. Ueda, J. Phys. Soc. Jpn. **73**, 2283 (2004).

Authors

T. Nakajima and Y. Ueda

Discovery of Metal-Insulator Transition in Hollandite Vanadium Oxide, $\text{K}_2\text{V}_8\text{O}_{16}$

Y. Ueda and Yagi Groups

We newly found a metal-insulator (MI) transition as a function of temperature in hollandite vanadium oxide, $\text{K}_2\text{V}_8\text{O}_{16}$. The MI transition has been a highlight in the strongly correlated electron system. Many compounds in the binary V-O system show MI transitions accompanied by the charge ordering and the formation of spin-singlet $\text{V}^{4+}\text{-V}^{4+}$ pairs. In the ternary systems, we recently discovered the charge order transition accompanied by the formation of spin gap and the devil's flower type phase diagram under high pressure in the 1/4-filled ladder insulator, NaV_2O_5 [1].

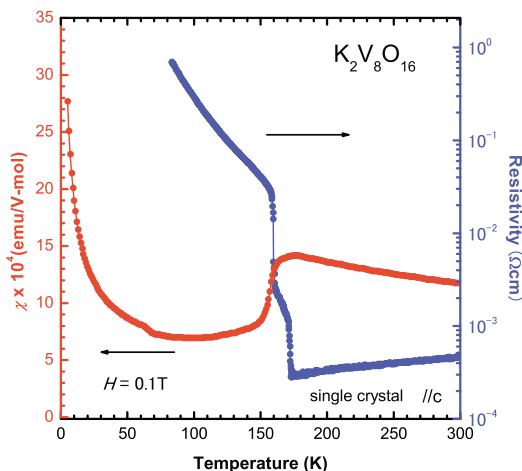


Fig. 1. Temperature dependences of resistivity and magnetic susceptibility for $K_2V_8O_{16}$.

Furthermore we found the MI transition as a function of temperature and the pressure-induced superconductivity in β -vanadium bronzes, $A_{0.33}V_2O_5$ ($A = Li, Na, Ag, Ca, Sr$) [2]. Vanadium oxides have been one of central materials in the study of strongly correlated electron system, as mentioned above.

We have engaged in the development of new vanadium oxides. The hollandite vanadium oxide, $K_2V_8O_{16}$ has been successfully synthesized by a solid state reaction under 4 GPa at 1473 K for 1 hour. Small crystals were also found in the sintered sample. By using single crystals we first found a metal-insulator (MI) transition with the two step jumps of resistivity about three orders around 170 K, as shown in Fig. 1. The transition is accompanied by a large reduction of magnetic susceptibility and a structure change from tetragonal to orthorhombic (or monoclinic). Single crystal X-ray diffraction study reveals a superlattice of $\sqrt{2} \times \sqrt{2} \times 2$ in the low-temperature insulator phase, suggesting a charge ordering. The reduction of magnetic susceptibility at the MI transition implies the formation of spin-singlet V^{4+} - V^{4+} pairs and V^{3+} - V^{3+} pairs. The structure of $K_2V_8O_{16}$ consists of V_8O_{16} -framework and K^+ located at the tunnel sites of V_8O_{16} -framework, as shown in Fig.2. The V_8O_{16} -framework is constructed from the double chains formed by sharing the edges of VO_6 octahedra. $K_2V_8O_{16}$ is a mixed valent oxide with a ratio of $V^{4+}/V^{3+} = 3/1$. We propose a possible charge ordered manner shown in Fig. 2. In this model, there exist two kinds of double-chain; the red one formed by V^{3+} and V^{4+} chains and the blue one formed by only V^{4+} chains. Each double-chain forms two kinds of tube with K^+ within each tube. The two tubes order in a manner

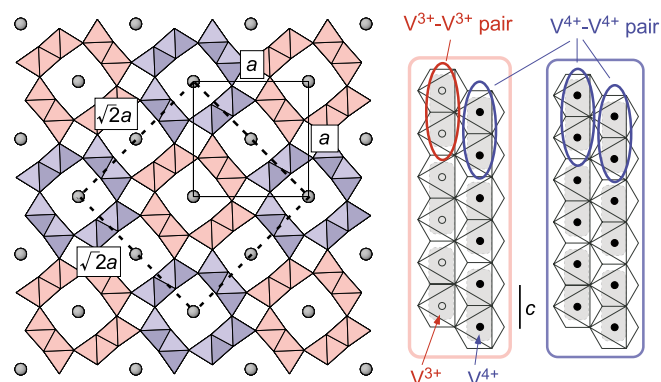


Fig.2. Schematic drawing of the crystal structure and the charge ordered pattern for hollandite vanadium oxide, $K_2V_8O_{16}$.

shown in Fig. 2, which satisfies a ratio of $V^{4+}/V^{3+} = 3/1$ and a superlattice of $\sqrt{2} \times \sqrt{2}$ in the a - b plane. The V^{4+} - V^{4+} and V^{3+} - V^{3+} pairs are formed in each chain along the c -axis, resulting in a duplication of the c -axis. The origin of the two stage transition has been open question. We also succeeded in synthesizing RbV_8O_{16} under the same conditions. RbV_8O_{16} shows a similar MI transition around 220 K accompanied by a similar reduction of magnetic susceptibility, but we have not observed any superlattice in RbV_8O_{16} .

References

- [1] K. Ohwada *et al.*, Phys. Rev. Lett. **87**, 086402 (2001).
- [2] T. Yamauchi, Y. Ueda, and N. Mori, Phys. Rev. Lett. **89**, 057002 (2002).

Authors

M. Isobe, N. Kouno, T. Yamauchi, J. Yamaura, H. Ueda, Y. Ueda, H. Gotou, and T. Yagi.

Complete Phase Diagram of Field Stabilized Novel Ferrimagnetic States Found in New Chromium Spinel $HgCr_2O_4$

Y. Ueda and Takeyama Groups

$HgCr_2O_4$ is a new member of chromium spinels. We found that this material is an antiferromagnet with a relatively small exchange constant. By applying magnetic field, the magnetic structure is easily adjusted; from antiferromagnet to ferrimagnetic state with three-up and one-down spin configuration, and then finally to ferromagnet.

Cubic normal spinels AB_2X_4 have a pyrochlore lattice as a B -sublattice. It is well-known that antiferromagnet on a pyrochlore lattice is a subject of strong spin frustration. For chromium spinels, magnetic Cr^{3+} ions have no orbital degen-

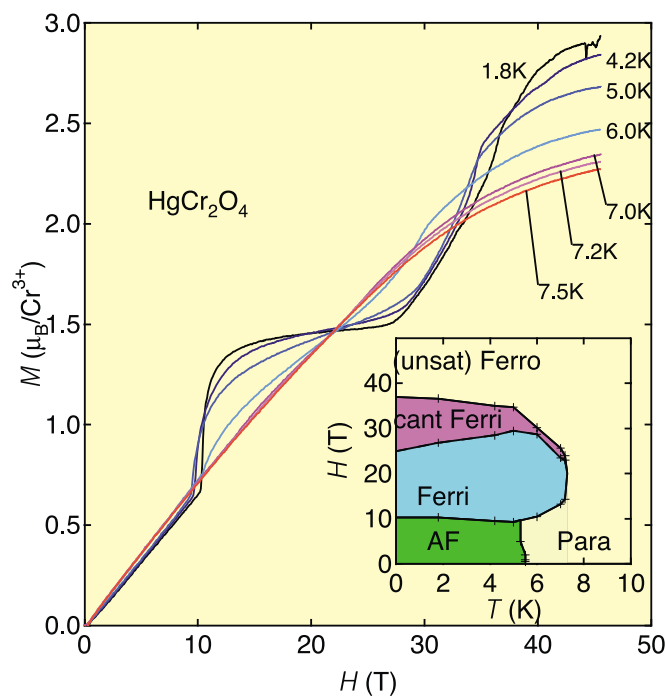


Fig. 1. Temperature dependence of magnetization curve for $HgCr_2O_4$. At low temperatures, a metamagnetic jump at 10T followed by a plateau region with one half moment and a kink about 35T are observed. Magnetization plateau phase with a half moment corresponds to three-up and one-down ferrimagnetic state, and the final state is ferromagnetic state. The inset shows complete H - T phase diagram of $HgCr_2O_4$. By applying high magnetic field, antiferromagnetic state goes into ferrimagnetic state and then ferromagnetic state.

eracy, indicating they are pure $S = 3/2$ Heisenberg spin system on a pyrochlore lattice. At low temperatures, antiferromagnetic orderings are marginally achieved with a help of structural distortion for ACr_2O_4 ($A = Mg, Zn, Cd$ and Hg). We might expect the formation of completely different spin ordering patterns and then different lattice distortions are realized by applying high magnetic field.

We have found a novel metamagnetic transition for $CdCr_2O_4$ at 28 T[1]. This transition field is too high for various measurements. Because of relatively small magnetic exchange energy for $HgCr_2O_4$, the whole feature of magnetization process is expected to be obtained. Magnetization curve of $HgCr_2O_4$ at 1.8K shows a discontinuous jump around 10 T, followed by a magnetization plateau as shown in the figure. A magnetization jump shows a hysteresis, indicating a first order transition, which is likely with a structural transition. The magnetic moment at the plateau is $1.5\mu_B$ per Cr^{3+} , which is exactly one half of the full moment of $S = 3/2 Cr^{3+}$. One half magnetization plateau can be assigned to a collinear three-up and one-down ferrimagnetic configuration. In addition to the half magnetization plateau, we found a transition to ferromagnetic state as a kink round 35T with hysteresis, indicating a second structural change.

These features can be visually summarized as a H - T phase diagram in the inset of the figure. Below $T_N = 5.8$ K, the range of ferrimagnetic state gradually expands, and then quickly diminishes above T_N . The robustness against temperature fluctuation suggests the collinear spin structure. Finite stable region at $T = 0K$ suggests spin-lattice coupling helps to stabilize this phase.

In summary, we can draw a complete H - T phase diagram of $HgCr_2O_4$, which indicates spin-lattice couplings and thermal fluctuation stabilize the novel three-up and one-down ferrimagnetic state.

Reference

[1] H. Ueda, *et. al.*, Phys. Rev. Lett. **94**, 047202 (2005).

Authors

H. Ueda, H. Mitamura, T. Goto, and Y. Ueda

3D Superfluidity and Vortex Physics of Thin He Films Formed on Prous Media under Fast Rotation

Kubota Group

Non-charged superfluids demand us special technology to study their unique properties. Recently we came across reports of new superfluidity found in quantum solid 4He [1] and possibly in other systems[2]. They are studied using a mechanical method, torsional oscillator technique, to detect the effective mass change of the container, which holds the sample. One of the common features in such systems as supersolid is their small superfluid density. This reflects rather long 3D coherence length of the system. Submonolayer superfluid 4He films condensed on flat substrates show ideal 2D KT transitions, whereas such films formed on 3D connected surfaces of porous media show also 3D transitions with rather small 3D superfluid density[3,4].

We have been studying superflow property[5] as well as torsional oscillator responses[6]. 3D vortex lines have been detected by our detailed torsional oscillator study[6]. They are signaled by the circulating superflow around pore vortex

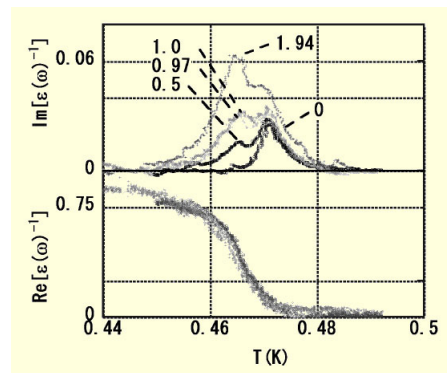


Fig. 1. Dissipation peaks and superfluid density for a He submonolayer superfluid film on $1 \mu m$ pore porous glass substrate, expressed in real and imaginary part of ϵ under rotation. The numbers refer to rev/sec.

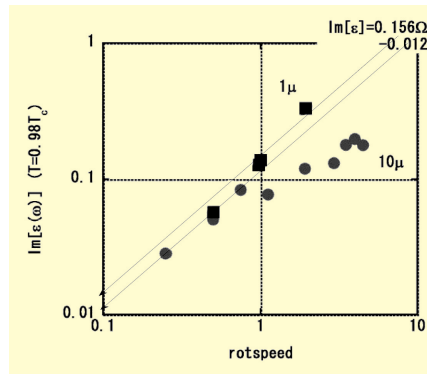


Fig. 2. Non-linear dependence of the rotation induced peak for $10 \mu m$ pore system, compared with $1 \mu m$ pore system linear dependence.

core. The flow field interacts with 2D vortices and dissipates energy and this gives information on the vortex line. The vortex core is modified by the pore size and we may expect non-linear behavior because of overlap of the cores under experimentally achievable conditions[7], which are impossible for the bulk superfluids, 4He and 3He .

Fig.1 shows TO result for submonolayer superfluid He film condensed on the pore surface of porous glass with controlled pore size of $1 \mu m$, expressed in terms of imaginary part as well as real part of "dielectric permeability" ϵ , which is the ratio of the effective mass of the superfluid component participating in the oscillation to the total or "bare" superfluid mass. The imaginary component indicates the energy dissipation caused by 2D vortices, compared with the real part, which is proportional to the superfluid mass. Under rotation we observe a new dissipation peak, whose height changes linearly with the rotational speed. This linear dependence is displayed in Fig. 2 for $1 \mu m$ system, whereas data for $10 \mu m$ pore diameter substrate with the same film thickness deviates from the linear dependence at rotational speed beyond 1 rev/sec, namely a non-linear behavior for the case of $10 \mu m$ pore system. We estimate the vortex line spacing and find out that this is actually happening because vortex lattice spacing approaches finite multiple of pore lattice average spacing.

We believe this is the first non-linear vortex phenomenon approaching Ω_{c2} , observed in a superfluid under rotation.

References

- [1] E. Kim and M. Chan, Nature **427**, 225 (2004); Science **305**, 1941 (2004).
- [2] see for example, H. Araki *et al.*, J. Low Temp. Phys. **134**, 1145 (2004).
- [3] T. Minoguchi and Y. Nagaoka, Prog. Theor. Phys. **80**, 397 (1988).
- [4] T. Obata and M. Kubota, Phys. Rev. B **66**, 140506(R) (2002).
- [5] M. Kubota *et al.*, J. Low Temp. Phys. **113**, 429 (1998).

- [6] M. Fukuda, M.K. Zhalutdinov, V. Kovacik, T. Minoguchi, T. Obata, M. Kubota, and E.B. Sonin, Phys. Rev. B **71**, 212502, (2005).
 [7] T. Obata, M. Fukuda, N. Mikhin, J. D. Reppy, and M. Kubota, J. Low Temp. Phys. **134**, 559-565 (2004).
 [8] T. Obata, I. Tanuma, T. Igarashi, and M. Kubota, J. Low Temp. Phys. **138**, 929-934 (2005); and to be published.

Authors

T. Obata, I. Tanuma, Y. Ito, T. Igarashi, E. Sonin^a, T. Minoguchi^b, and M. Kubota

^aRacah Institute of Physics, Hebrew University of Jerusalem
^bInst.on Physics. University of Tokyo, Komaba, Tokyo

Vortex State of ³He-A under Rotation up to 1 rev/sec Speed, Studied by the Main NMR Line Width Change

Kubota Group

Vortex state of the unique system of superfluid ³He has been studied under rotation for many years. In the anisotropic superfluid ³He-A, there have been four different vortex states experimentally reported. The vortex state has been studied most commonly by torsional oscillator technique and by NMR techniques. Since the earliest NMR experiment, in addition to the appearance of vortex satellite peak, the main NMR line width in the A phase was realized to be broadened under rotation. A unique theoretical work by Fomin and Kamenskii(1982) predicted three different temperature ranges where NMR line width change under rotation to show different dependences on the reduced temperature by considering spin diffusion constant change in the vicinity of Tc and spin wave velocity at the lowest temperature range. In between they predicted a plateau of the line width change as a function of the reduced temperature. Experimental work has been reported by Helsinki Group, Eltsov *et al.*(2001) and references therein. As is discussed by Eltsov *et al.*, the most common vortex in ³He-A is Continuously Unlocked Vortex (CUV). So far the predicted three temperature ranges have not observed in experimental study.

We report our NMR line width measurements and discuss the three distinct temperature ranges where we could obtain different features under rotation up to 1 rev/sec speed, which had not been realized till present study.

Fig. 1. illustrates an example of temperature sweep under the highest rotational speed of 6.28 rad/sec. We made such

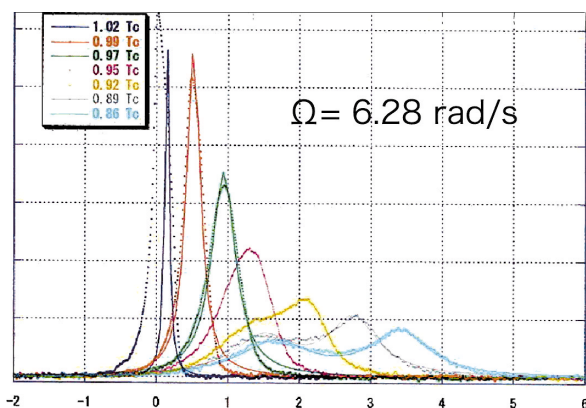


Fig. 1. NMR spectrum (as a function of frequency shift in kHz from Larmor frequency.) of superfluid ³He-A under the world record rotational speed of 6.28 rad/sec for different temperatures over the A phase at P=30 bar. We observe the frequency shift and line broadening as temperature decreases. In addition, another satellite peak (so called vortex peak) appears at a constant frequency.

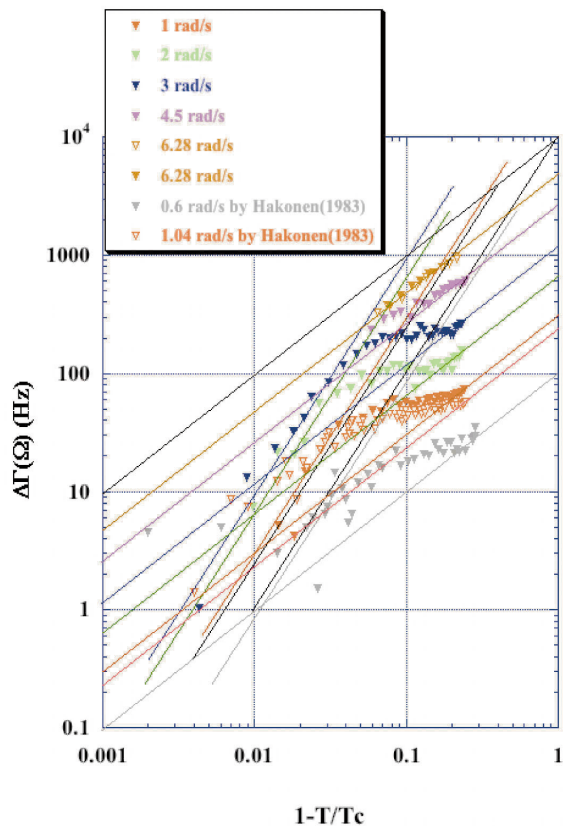


Fig.2. ³He-A main line width change as a function of reduced temperature for different rotational speed given in rad/sec.

measurements also at 4.5, 3, 2, 1rad/sec speed and further we made rotational speed Ω sweeps at fixed temperatures. Fig. 2. indicates rather clearly the different reduced temperature $\tau = 1 - T/T_c$ dependence changes predicted in the old theory[1], but the linear rotational speed dependence was realized only at the lowest temperature (highest τ) region. Since the NMR line width is determined by dynamical features of spin(d) as well as mass (angular momentum l) freedom of the order parameter of ³He-A, further related study is necessary.

References

- [1] I.A. Fomin and V.G. Kamenskii, JETP Lett. **35**, 302 (1982).
 [2] V.B. Eltsov, R. Blaauwgeers, M. Krusius, J.J. Ruohio, and R. Schanen, J. Low Temp. Phys. **124**, 123 (2001).

Authors

Y. Kataoka, M. Yamashita^a, K. Izumina, O. Ishikawa^b, and M. Kubota
^aGrad School, Phys. Kyoto Univ.
^bPhys. Dept. Osaka City Univ